JACS
JOURNAL OF THE AMERICAN CHEMICAL SOCIETY
pubs.acs.org/JACS

Article

ATP-Triggered $Fe(CN)_2CO$ Synthon Transfer from the Maturase HypCD to the Active Site of Apo-[NiFe]-Hydrogenase

Anna Kwiatkowski, Giorgio Caserta,* Anne-Christine Schulz, Stefan Frielingsdorf, Vladimir Pelmenschikov, Kilian Weisser, Adam Belsom, Juri Rappsilber, Ilya Sergueev, Christian Limberg, Maria-Andrea Mroginski, Ingo Zebger, and Oliver Lenz*

Cite This: J. Am. Chem. Soc. 2024, 146, 30976−30989

Read Online

ACCESS | Metrics & More | Article Recommendations | Supporting Information

ABSTRACT: [NiFe]-hydrogenases catalyze the reversible activation of H_2 using a unique $NiFe(CN)_2CO$ metal site, which is assembled by a sophisticated multiprotein machinery. The [4Fe−4S] cluster-containing HypCD complex, which possesses an ATPase activity with a hitherto unknown function, serves as the hub for the assembly of the $Fe(CN)_2CO$ subfragment. HypCD is also thought to be responsible for the subsequent transfer of the iron fragment to the apo-form of the catalytic hydrogenase subunit, but the underlying mechanism has remained unexplored. Here, we performed a thorough spectroscopic characterization of different HypCD preparations using infrared, Mössbauer, and NRVS spectroscopy, revealing molecular details of the coordination of the $Fe(CN)_2CO$ fragment. Moreover, biochemical assays in combination with spectroscopy, AlphaFold structure predictions, protein−ligand docking calculations, and crosslinking MS deciphered unexpected mechanistic aspects of the ATP requirement of HypCD, which we found to actually trigger the transfer of the $Fe(CN)_2CO$ fragment to the apo-hydrogenase.

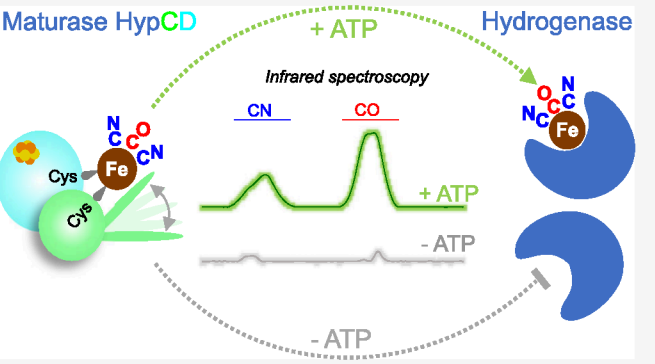

INTRODUCTION

By making use of earth-abundant nickel and iron ions, [NiFe]-hydrogenases catalyze the reversible activation of H_2 close to the thermodynamic potential under ambient conditions.[1] The functional unit of [NiFe]-hydrogenases features a bipartite architecture consisting of a catalytically competent large subunit that carries the heterobimetallic $NiFe(CN)_2CO$ active site and a small subunit, which contains one to three Fe−S clusters acting as an electric wire. The synthesis and assembly of the $NiFe(CN)_2CO$ cofactor requires an intricate protein machinery comprising at least six Hyp proteins named HypA−F.[2−5] The current biosynthesis model envisages the [4Fe−4S] cluster-containing HypCD protein complex as a hub for the assembly of the $Fe(CN)_2CO$ synthon of the catalytic site (Figure S1). The CN^- strong field ligands are synthesized from carbamoylphosphate by the maturases HypF and HypE[6] and are supposed to be transferred by the latter to a single iron ion transiently bound by HypCD. The aerobic biosynthesis of the CO ligand from N^{10}-formyl-tetrahydrofolate has recently been uncovered,[7,8] while the corresponding anoxic pathway remains elusive.[9,10] The assembled $Fe(CN)_2CO$ synthon is then transferred to the apo-form of the large hydrogenase subunit via an unknown mechanism. Only then do the maturases HypA and HypB complete the active site metalation by mediating the insertion of a Ni ion.[11] Finally, the fully metalated hydrogenase large subunit is usually processed by endoproteolytic cleavage of its C-terminal extension.[12−14] This step has been shown to trigger structural changes at the NiFe site (e.g., incorporation of an OH^- ligand bridging Ni and Fe),[15] which also allows the association of the large and small subunits to form catalytically competent [NiFe]-hydrogenase.[13]

Although the biosynthesis of the NiFe site has been examined in great detail,[15,16] several aspects of the maturation process are still unclear. Among them, the mechanism by which the $Fe(CN)_2CO$ fragment is transferred from the HypCD complex to the apo-large subunit is essentially unknown. Recent work from the Sawers group has revealed an unexpected ATPase activity of the HypCD complex.[17,18] Although the role of ATP hydrolysis in either the biosynthesis of the CO ligand or the transfer of the $Fe(CN)_2CO$ unit into the large subunit of the hydrogenase was hypothesized, there

Received: July 18, 2024
Revised: October 19, 2024
Accepted: October 21, 2024
Published: November 4, 2024

https://doi.org/10.1021/jacs.4c09791
J. Am. Chem. Soc. 2024, 146, 30976−30989

was no experimental evidence for this and for a possible ATP binding site.

In the present study, we extend our knowledge of [NiFe]-hydrogenase maturation to new aspects. We developed an *in vitro* assay with purified HypCD from *Escherichia coli* and the apo-large subunit HoxC of the regulatory [NiFe]-hydrogenase (RH) from *Cupriavidus necator* to investigate the role of the ATPase activity of HypCD in hydrogenase maturation. To this end, we first comprehensively characterized the purified HypCD complex by infrared (IR) and Mössbauer spectroscopy, which verified the integrity and stoichiometric loading with the $Fe(CN)_2CO$ synthon. Nuclear resonance vibrational spectroscopy (NRVS) in combination with density functional theory (DFT) provided details of the synthon bonding and a realistic structural model of holo-HypCD, which is consistent with the available biochemical and spectroscopic data. Protein−ligand docking calculations revealed that the most probable binding site of ATP overlaps with the proposed binding site of the $Fe(CN)_2CO$ synthon in HypCD. Using the *in vitro* transfer assay, we were able to probe and elucidate the role of ATP, showing that nucleotide binding triggers the transfer of the $Fe(CN)_2CO$ synthon from purified holo-HypCD to an apo-large subunit of the hydrogenase. AlphaFold-based structure predictions in combination with crosslinking mass spectrometry (crosslinking MS) indicate ATP-dependent structural changes within the HypCD complex. From these results, we developed a molecular model for the ATP-mediated transfer of the $Fe(CN)_2CO$ synthon to the apo-form of the hydrogenase large subunit.

RESULTS AND DISCUSSION

Isolation and Spectroscopic Characterization of the HypCD and HoxC Proteins. Holo- and apo-$HypC_{Strep}$-HypD protein complexes (Strep-tag II C-terminally fused to HypC hereafter referred to as holo- and apo-$HypC_S$-D) were isolated by Strep-Tactin-based affinity chromatography from soluble extracts (Table S1) of aerobically cultivated *E. coli* (*Ec*) cells carrying $pTHypDC_{Strep}$ and $pTHypDEFC_{Strep}$ expression plasmids (Table S2).[19,20] SDS-PAGE analysis of the isolated protein complexes showed the typical bands for HypC and HypD (Figure S2), which is consistent with previous studies.[19] Apo-$_{Strep}$HoxC (apo-$_S$HoxC; Strep-tag II N-terminally fused to HoxC) from *Cupriavidus necator* (*Cn*) was heterologously overproduced in *E. coli* cells bearing the expression plasmid pTS17 (Table S2) and also isolated via Strep-Tactin-based affinity chromatography. The isolated proteins (complexes) were characterized by IR spectroscopy in the 2150−1800 cm^{-1} range to verify the presence of CO and CN^- ligands usually observed in hydrogenase maturation intermediates and fully assembled [NiFe]-hydrogenases.[1,15] Clear IR absorption signals were exclusively detected for holo-$HypC_S$-D (Figure S3). The observed ν_{CN} bands at 2098 and 2072 cm^{-1} and ν_{CO} bands at 1951 and 1963 cm^{-1} resemble those previously reported,[20,21] suggesting the isolation of a native-like HypCD complex. The metal content of $HypC_S$-D was then determined by inductively coupled plasma-optical emission spectroscopy (ICP-OES). The iron content of holo-$HypC_S$-D was determined with 6.64 ± 0.09 and that of apo-$HypC_S$-D with 5.37 ± 0.06. For unknown reasons, the total iron content of both proteins exceeds the theoretical iron content by 1−1.5 iron. Importantly, both proteins differed as expected by about one iron ion, which can presumably be assigned to the species equipped with the CO/CN^- ligands (see below). To test whether both HypD and HypC are required for assembly and binding of the $Fe(CN)_2CO$ fragment, we purified the two proteins independently, and the corresponding IR measurements did not reveal any detectable CO/CN^- absorptions (Figure S4). These data, therefore, strongly suggest that the assembled holo-HypCD complex is required for $Fe(CN)_2CO$ fragment synthesis.

Characterization of the $Fe(CN)_2CO$ Fragment in HypCD. The $Fe(CN)_2CO$ fragment of the hydrogenase active site has been shown to be EPR-silent, which has been interpreted as a Fe^{II} low-spin configuration.[1] Previous Mössbauer data on holo-HypCD showed small resonance signals attributed to a low-spin Fe^{II} species, but their origin was not confirmed by measurements on an apo-HypCD construct without the $Fe(CN)_2CO$ synthon.[22] Therefore, we recorded zero-field Mössbauer spectra for both apo- and holo-$HypC_S$-D enriched with ^{57}Fe (see the Methods section). Resonance signals of both samples were simulated with different spectral components, which are shown in Figure 1a,b. The main signals in both holo- and apo-$HypC_S$-D are typical of a quadrupole doublet consisting of two components, each representing a $Fe^{2.5+}-Fe^{2.5+}$ pair of a $[4Fe-4S]^{2+}$ cluster. The isomer shifts and quadrupole splitting parameters are given in Table S3. The parameters of the [4Fe−4S] cluster in both apo- and holo-$HypC_S$-D are almost identical to those previously reported.[22,23] Besides minor signals of a $[3Fe-4S]^+$ species,[24] the fit used to simulate the apo-$HypC_S$-D spectrum did not require any additional spectral components. In contrast, holo-$HypC_S$-D contains an additional and significant resonance characterized by an isomer shift of δ = 0.25 mm s^{-1} and a quadrupole splitting of ΔE_Q = 1.60 mm s^{-1}. For [NiFe]-hydrogenases, these parameters have been associated with a 5-fold coordinated low-spin Fe^{II} species equipped with one CO and two CN^- ligands.[22,25] The intensity of this resonance appears considerably higher than that previously reported,[22] indicating a significantly higher (^{57}Fe) occupancy of the low-spin Fe^{II} species in our protein preparations. Our data show that both the [4Fe−4S] cluster and the $Fe(CN)_2CO$ synthon are incorporated stoichiometrically into HypCD, even under aerobic conditions.

To shed light on the coordination of iron ions, we employed nuclear resonance vibrational spectroscopy (NRVS). This synchrotron technique provides vibrational dynamics for Mössbauer-active nuclei, such as the ^{57}Fe isotope. Typical NRVS data of [NiFe]-hydrogenases comprise dominant Fe−S stretching and bending modes (100−420 cm^{-1}) of the [Fe−S] clusters of the small subunit as well as Fe−CO/CN stretching and bending modes of the NiFe active site (400−650 cm^{-1}).[26,27]

Depending on the (redox) state of the active site, modes of bridging hydride and hydroxide ligands have also been assigned.[28,29] Apo-$HypC_S$-D predominantly showed signals that can be assigned to a [4Fe−4S] cluster (Figure 1c). Major bands were detected at 150 cm^{-1} (bending and breathing modes of the cluster), as well as at 275, 366, and 385 cm^{-1}, which represent normal modes with predominant Fe−S stretching character. These signals appeared at positions similar to those observed for the [4Fe−4S] cluster-containing ferredoxin (D14C variant) from *Pyrococcus furiosus*.[30] Holo-$HypC_S$-D, on the other hand, exhibited additional absorptions at 438, 501, 589, and 620 cm^{-1}, which originate from modes involving the CO/CN^- ligands of the $Fe(CN)_2CO$ synthon (see next paragraph). In conclusion, our Mössbauer and NRVS

https://doi.org/10.1021/jacs.4c09791
J. Am. Chem. Soc. 2024, 146, 30976−30989

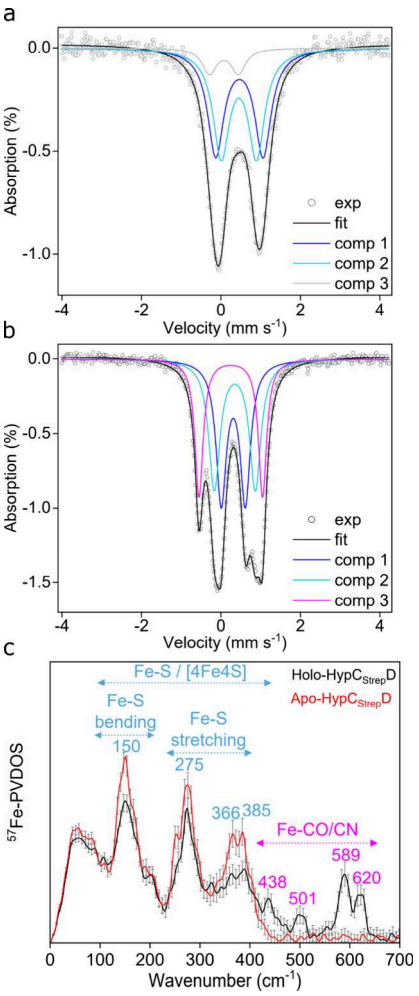

Figure 1. Mössbauer and NRVS characterization of apo- and holo-HypCD. Experimental Mössbauer data for (a) apo- and (b) holo-HypCD are depicted as single data points (circles). Black lines correspond to the curve fits containing all spectral components; the dark blue (component 1) and light blue (component 2) lines correspond to the two $Fe^{2.5+}$–$Fe^{2.5+}$ pairs of the $[4Fe–4S]^{2+}$ cluster. The gray line (component 3) in panel a represents the spectral contribution of a [3Fe–4S] cluster (minor) in apo-HypCD. The magenta line in panel b corresponds to the $Fe^{II}(CN)_2CO$ species in holo-HypCD. (c) NRVS of apo-HypCD (red trace) showing Fe–S bending/stretching bands originating from the [4Fe–4S] cluster (blue dashed arrows). The contribution of the $Fe(CN)_2CO$ fragment is detectable only in the holo-HypCD spectrum (black trace), characterized by bands in the Fe–CN/CO region (magenta dashed arrow).

data convincingly show that holo-HypCD harbors two iron cofactors, a [4Fe–4S] cluster and a low-spin $Fe^{II}(CN)_2CO$ fragment. Strikingly, the high-frequency region of the NRVS spectrum in holo-$HypC_S$-D resembles that of the nickel-free maturation intermediate of the membrane-bound hydrogenase (MBH) large subunit from *C. necator*[15] (Figure S5). This intermediate has been shown to bind a 5-fold coordinated $Fe(CN)_2CO$ fragment, presumably via two of the four conserved cysteine residues of the hydrogenase active site. Given the similarity of the high-frequency spectral range of the two proteins, a comparable coordination can be inferred for the $Fe^{II}(CN)_2CO$ species in both holo-HypCD and the nickel-free large hydrogenase subunit. This scenario is in agreement with prior computational and biochemical data suggesting that the $Fe(CN)_2CO$ fragment in HypCD is coordinated by one cysteine residue from HypC and one from HypD.[31,32]

Binding Site of the $Fe(CN)_2CO$ Fragment in HypCD. The binding of the $Fe(CN)_2CO$ cofactor in *Ec*HypCD was further analyzed using density functional theory (DFT) calculations (see the Methods section). We adopted the previously proposed low-spin ferrous Fe^{II} center coordination by the thiolates of $Cys2_{HypC}$ and $Cys41_{HypD}$ (Figure 2a)[31,32] as a constraint for our DFT modeling. The protein environment of the $Fe(CN)_2CO$ fragment was based on the cofactor-free AlphaFold structure of *Ec*HypCD generated as described in the

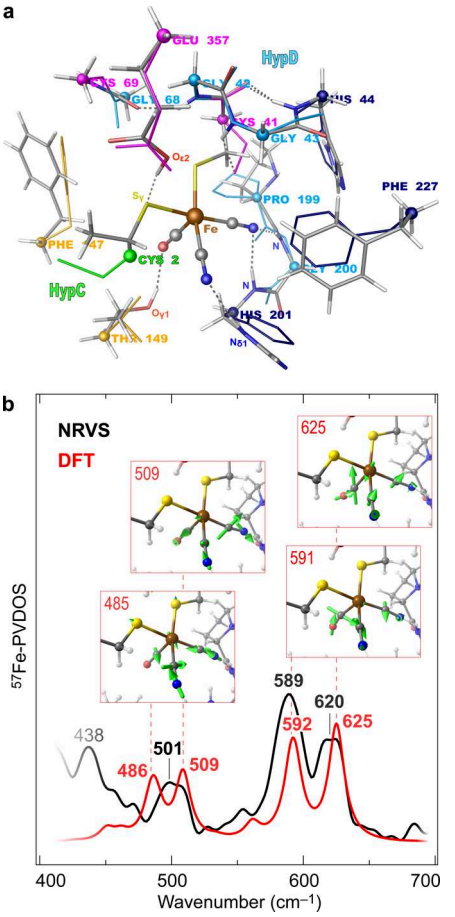

Figure 2. DFT modeling of the $Fe(CN)_2CO$ cofactor binding site in *Ec*HypCD and the corresponding NRVS spectrum. (a) The optimized DFT structure (tube representation, element colors) is overlaid with the original positions of the amino acid residues in the apo-*Ec*HypCD AlphaFold model (wire representation). The color codes for the reference residues of the AlphaFold model are as follows: HypC: Cys2, light green. HypD: Cys41/Cys69/Glu357, important for the assembly of the $Fe(CN)_2CO$ cofactor,[32,33] magenta; Phe147/Thr149 of the conserved $GF_{147}ET_{149}T$ motif, orange; His44/His201/Phe227 matching three residues within 3 Å from the cofactor in the *Tk*HypCD model by Albareda et al.,[31] dark blue; Gly42/Gly43/Gly68/Pro199/Gly200, light blue. Individual atoms participating in hydrogen bonding (···) with the cofactor are named. C_α and $Fe(CN)_2CO$ fragment atoms are shown as spheres. (b) Predicted (DFT, red trace) and experimental (NRVS, black trace) ^{57}Fe-PVDOS of holo-*Ec*HypCD in the 400–700 cm^{-1} spectral range. Selected vibrational modes are shown in an arrow-style representation above the spectra. Animations of these and other normal modes are available as part of the Supplementary Data III. An extended version of panel b is available in Figure S7.

https://doi.org/10.1021/jacs.4c09791
J. Am. Chem. Soc. 2024, 146, 30976–30989

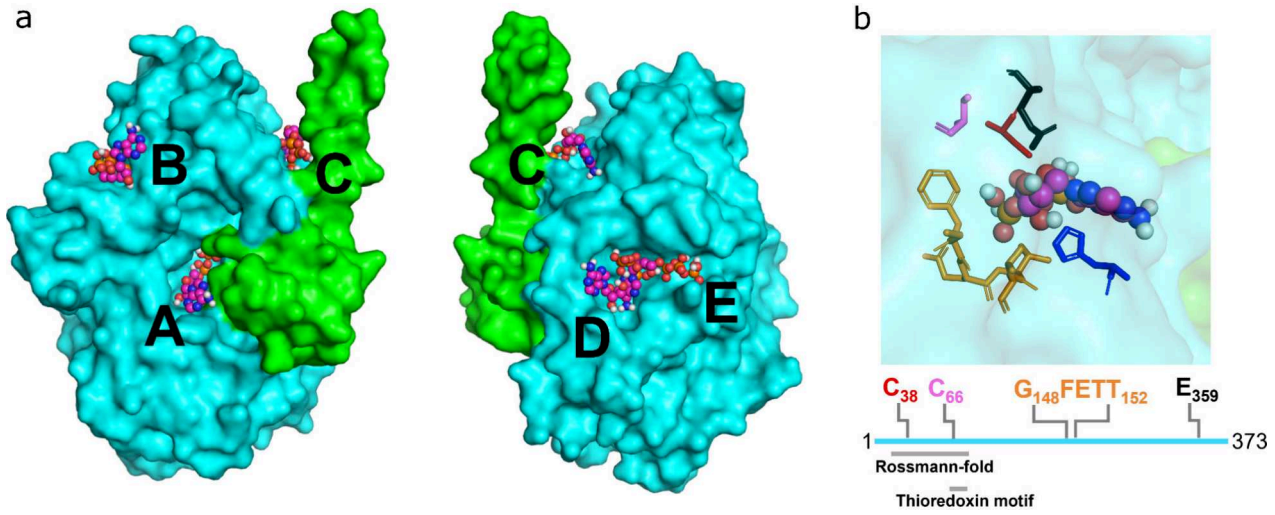

Figure 3. Predicted docking sites for ATP in *T. kodakarensis* HypCD. (a) ATP-binding locations as predicted by CB-Dock2 are labeled alphabetically (A–E). Vina Scores: Cavity A, −8.3; B, −5.7; C, −6.3; D, −5.5; E, −5.9. HypD is depicted in cyan, and HypC is in green. ATP is shown as spheres. (b) Close-up of the predicted connection residues to ATP in cavity A, including the conserved residues Cys38 (red), Cys66 (magenta), and Glu359 (black) from HypD and His45 (blue) from HypC.[32,33,37,38] The highly conserved GFETT motif (orange) in HypD (Figures S10 and S11) is also part of cavity A, with connections to the ATP molecule. A representation of the amino acid sequence of HypD illustrates the affiliation of individual amino acid residues to the Rossman fold and/or the thioredoxin motif (gray bars) of HypD.

Methods section. Notably, the incorporation of the Fe(CN)$_2$CO fragment was achieved without apparent steric clashes. Only moderate changes in the amino acid side chain positions were produced by the subsequent DFT structure optimization. The refined model of holo-*Ec*HypCD in comparison to the initial AlphaFold structure is shown in Figure 2a and Figure S6 (with conserved motifs of HypD highlighted). The position of the Fe(CN)$_2$CO synthon in *Ec*HypCD is reminiscent of that in a previous model of holo-HypCD from *Thermococcus kodakarensis* (*Tk*).[31,32] In our model, the diatomic CN^- and CO ligands form hydrogen bonds with HypD residues His201, Gly200, and Thr149. Furthermore, Glu357 from HypD forms a hydrogen bond with the sulfur atom of Cys2 from HypC (Figure 2a). The specific contacts are $(C_2)S_\gamma\cdots H{-}O_{\varepsilon 2}(E_{357})$ = 3.08 Å, $CN\cdots H{-}N_{\delta 1}(H_{201})$ = 2.87 Å, $CN\cdots H{-}N(H_{201}/G_{200})$ = 3.18/2.91 Å, and $CO\cdots H{-}O_{\gamma 1}(T_{149})$ = 2.99 Å.

The DFT model of holo-*Ec*HypCD was also used to simulate the ^{57}Fe-PVDOS (partial vibrational densities of states) contribution of the Fe(CN)$_2$CO fragment to the NRVS spectrum discussed above and shown in Figure 1c. Figure 2b shows that the calculations reproduce the high-energy spectral region from 450 to 650 cm^{-1}, which contains mixed modes of predominantly stretching Fe–CO/CN and bending Fe–C–O/N characters. The two modes of the strongest symmetric/antisymmetric Fe–S($Cys2_{HypC}$/$Cys41_{HypD}$) stretching character were calculated at 390 and 366 cm^{-1} (Figure S7). Interestingly, these Fe–S modes of the cysteine-bound Fe(CN)$_2$CO cofactor produce only very low ^{57}Fe-PVDOS intensities, in contrast to the corresponding vibrational energy regions of Fe–S clusters[30] such as the $[4Fe{-}4S]^{2+}$ cubane of HypCD (Figure 1c and Figure S5). Thus, our normal-mode analysis suggests that the principal Fe–S stretches of holo-*Ec*HypCD are associated with *rotations* of the FeC_3 core instead of *displacements* of the Fe center. The presence of "NRVS-silent" Fe–S stretches in holo-*Ec*HypCD agrees well with the intensity level near the baseline around 350–400 cm^{-1} of the nickel-free hydrogenase large subunit intermediate[15] (Figure S5), which is expected to bind the Fe(CN)$_2$CO fragment in a similar manner as HypCD (see above).

ATP Binding Site in HypCD. Both the apo- and holo-forms of anaerobically purified HypCD and the paralogous HybG–HypD complex from *E. coli* have been shown to hydrolyze ATP.[17,18] However, the ATP binding site and the biological function of ATPase activity remained unknown. To shed light on the possible binding site for ATP in HypCD, protein–ligand docking simulations were performed using CB-Dock2[34,35] and the crystallographic coordinates of apo-*Tk*HypCD (PDB: 3VYR).[32] CB-Dock2 performs docking in each cavity of the protein of interest and ranks the cavities according to the best Vina score—an empirical parameter related to the free binding energy. The more negative the score, the more reliable the result. For *Tk*HypCD, CB-Dock2 calculated five different docking sites for ATP (cavities A–E, Figure 3a). Cavity A was found to have the lowest Vina score of −8.3, making it the most favorable binding site for ATP in HypCD. To test the validity of CB-Dock2, we calculated the ATP docking sites in the hydrogenase maturase HypE, which has been shown to bind and hydrolyze ATP for CN^- ligand synthesis.[6]

In fact, the ATP-HypE docking data with the lowest Vina score of −8.7 corresponds to the experimentally determined binding site of the nucleotide in HypE[36] (Figure S8a,b and Table S4). We also calculated the electrostatic charge distribution in *Tk*HypCD at pH 7.0. The surface corresponding to cavity A is strongly positively charged, making it prone to the binding of negatively charged molecules such as ATP (Figure S9). Besides determining various docking locations, CB-Dock2 also discloses the amino acid side chains surrounding the docked ligand (Table S5). For cavity A, amino acid (aa) residues of both HypC and HypD are listed as the connecting residues. These include $Cys38_{HypD}$ and $Cys66_{HypD}$ (*Tk* numbering, Figure 3b), which have been shown to be crucial for the ATPase activity for HypCD and HybG-HypD as well as for the maturation of the hydrogenases I–III from *E. coli*.[33] The nearby residues also include the

https://doi.org/10.1021/jacs.4c09791
J. Am. Chem. Soc. 2024, 146, 30976–30989

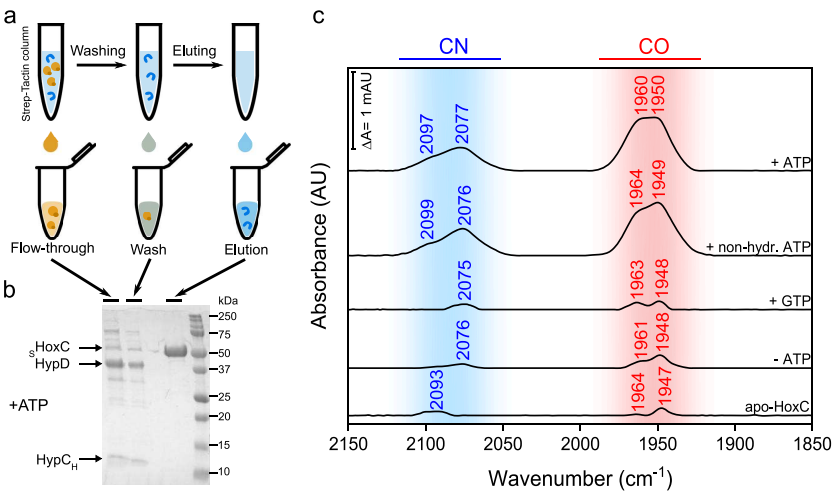

Figure 4. *In vitro* transfer assays using holo-HypCD and apo-HoxC proteins. (a) Schematic representation of the $Fe(CN)_2CO$ transfer assay using holo-$HypC_H$-D (orange) and apo-$_S$HoxC (blue). (b) SDS-PAGE analysis of purified $_S$HoxC after the transfer reaction in the presence of ATP (see Figure S16 for SDS-PAGE analysis for the transfer reactions with other nucleotides). (c) IR spectra of purified $_S$HoxC proteins after the transfer reaction with different nucleotides. CO and CN^- absorptions in panel c are labeled with the corresponding wavenumbers. The spectra are normalized with respect to the amide II band intensity. Three independent experiments were performed for each transfer assay, of which one representative IR spectrum (panel c) and one SDS-PAGE (panel b and Figure S16) are shown.

GFETT motif (residues $148-152_{HypD}$), which is highly conserved in HypDs from different species (Figures S10 and S11). When comparing the HypCD docking data for ATP (Figure 3) and the DFT model for the $Fe(CN)_2CO$ fragment (Figure 2a), it appears that the same protein cleft accommodates both cofactors. In fact, Cys38 of *Tk*HypCD (analogous to Cys41 in *Ec*HypCD) is predicted to be located at hydrogen-bonding distance (ca. 3 Å) from ATP (Figure 3b), and its thiolate side group is proposed to be one of the two protein ligands of the $Fe(CN)_2CO$ fragment.[31,32,37]

HypCD Uses ATP to Transfer the $Fe(CN)_2CO$ Synthon to the Apo-Hydrogenase. As outlined above, CB-Dock2 data predicted a docking site for ATP in *Tk*HypCD in proximity to residues proposed to bind the $Fe(CN)_2CO$ fragment. Considering that both apo- and holo-HypCD from *E. coli* have been shown to hydrolyze ATP,[17,18] it has been hypothesized that ATP might play a role either in the assembly of the $Fe(CN)_2CO$ fragment (e.g., synthesis of the CO ligand)[22] or in the transfer of the $Fe(CN)_2CO$ moiety to the apo-form of the large hydrogenase subunit. Our HypCD preparations harbor the $Fe(CN)_2CO$ fragment in stoichiometric quantities and can hydrolyze ATP as shown by a biochemical (coupled) assay using pyruvate kinase (PK) and lactate dehydrogenase (LDH) and IR spectroscopy (Supplementary Note and Figures S12 and S13a,b). To investigate whether ATP plays a role in the transfer of the $Fe(CN)_2CO$ fragment, we designed an *in vitro* assay using holo-HypCD and the apo-form of the large subunit HoxC of the regulatory hydrogenase from *C. necator*. First, we genetically replaced the C-terminal Strep-tag II at HypC in holo-HypCD with a hexa-His affinity tag (Table S2), resulting in holo-$HypC_H$-D. UV–vis and IR measurements (Figures S14 and S15) revealed almost identical spectra for holo-$HypC_H$-D and holo-$HypC_S$-D indicating that the former is fully equipped with a [4Fe–4S] cluster and the $Fe(CN)_2CO$ synthon. We then incubated holo-$HypC_H$-D, ATP (and other nucleotides, see Table S6), and apo-$_S$HoxC (Strep-tag II N-terminally fused to HoxC) under anoxic conditions as described in the Methods. After incubation for 1 h, $_S$HoxC was repurified by Strep-Tactin affinity chromatography (Figure 4a,b, and Figure S16) and subsequently subjected to IR spectroscopy to verify that the $Fe(CN)_2CO$ fragment was transferred to the apo-large subunit. The results are summarized in (Figure 4c). ATP turned out to be essential for the transfer of the $Fe(CN)_2CO$ synthon. Prominent IR absorption bands were observed in HoxC when ATP was present in the reaction mixture (+ATP), while negligible CO/CN^--related signals were observed when ATP was omitted (−ATP).

Such minor absorption bands were also observed for highly concentrated apo-HoxC protein solutions and are likely due to the endogenous Hyp machinery in the *E. coli* Rosetta (DE3) strain used to produce apo-HoxC. Although these data may suggest that hydrolysis of ATP is necessary for the transfer of the $Fe(CN)_2CO$ fragment to the large subunit, this does not appear to be the case, as the non-hydrolyzable ATP analogue *β,γ*-methyleneadenosine 5′-triphosphate (non-hydr. ATP) also enables efficient cofactor transfer (Figure 4c). An additional control experiment with GTP (instead of ATP), although slowly hydrolyzed by HypCD (Figure S13c), also resulted in negligible CO/CN^--related absorption bands in $_S$HoxC, thus confirming the necessity of adenine nucleotides. Since holo-HypCD did not hydrolyze *β,γ*-methyleneadenosine 5′-triphosphate, as shown by IR spectroscopy (Figure S13d), we conclude that the binding of ATP, and not its hydrolysis, is required to transfer the $Fe(CN)_2CO$ fragment. It is important to note that the IR spectrum of the *in vitro* matured HoxC resembles that of preHoxG$^{\Delta Ni}$ (Figure S17), a maturation intermediate of a [NiFe]-hydrogenase large subunit purified from living cells, which exclusively carries the $Fe(CN)_2CO$ unit.[15] This indicates that our *in vitro* assay enables the incorporation of the $Fe(CN)_2CO$ synthon into apo-HoxC in a native way.

ATP Triggers Displacements of the C-Terminal Part of HypC. In this study, we employed the holo-HypCD complex from *E. coli* for the *in vitro* transfer experiments. Considering the lack of an atomic structure, we used AlphaFold 2 to predict the *Ec*HypCD complex (Figure 5a and Figure S18). A comparison of the predicted *Ec*HypCD

https://doi.org/10.1021/jacs.4c09791
J. Am. Chem. Soc. 2024, 146, 30976–30989

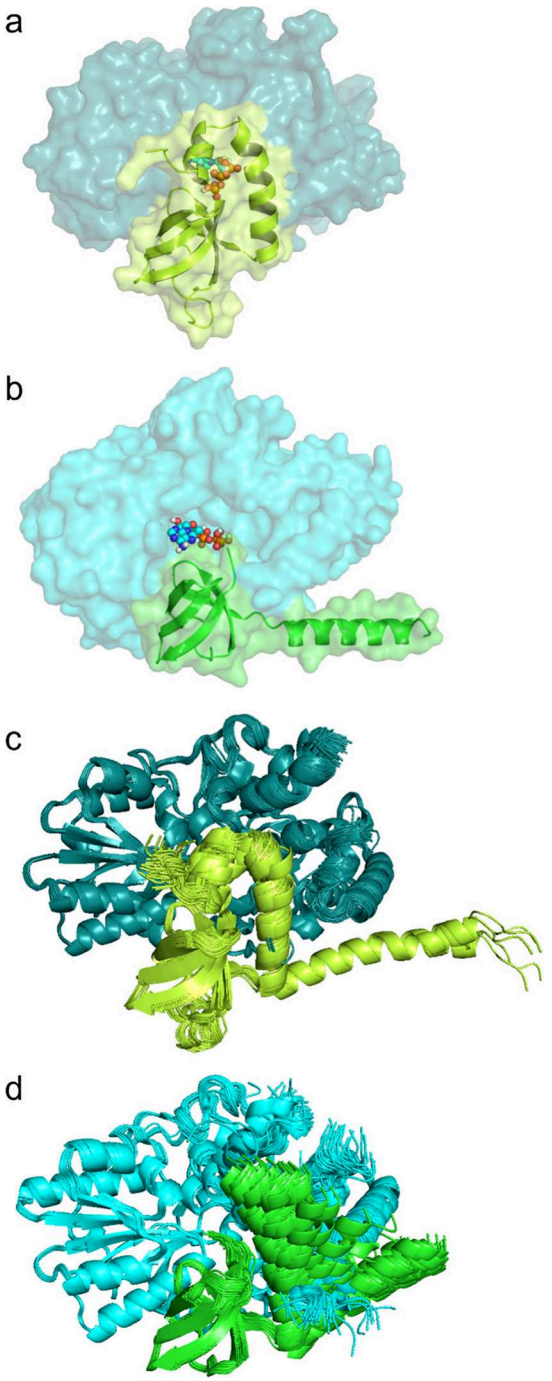

Figure 5. Different conformations of the C-terminal part of HypC in *Ec*HypCD and *Tk*HypCD structure predictions. (a) AlphaFold-predicted "closed conformation" of *Ec*HypCD. The C-terminal part of HypC covers the ATP-binding pocket (ATP is shown in sphere representation). (b) "Open conformation" of the *Tk*HypCD crystal structure. The C-terminal, mostly helical part of HypC bends away from the HypCD complex, exposing the ATP/$Fe(CN)_2CO$-binding pocket. HypD is shown in panels a and b in the surface representation (shades of blue), while the different conformations of HypC (shades of green) are displayed in the cartoon representation for clarity. (c) Overlay representation of various structures predicted by AlphaFold 2 for *Ec*HypCD using different presettings. (d) Overlay representation of various structures predicted by AlphaFold for *Tk*HypCD using different presettings. Note that the C-terminal part of HypC can adopt different positions, including the "open" and the "closed", while the rest of the HypCD complexes remain almost unchanged.

with the X-ray crystal structure of *Tk*HypCD (PDB: 3VYR)[32] is shown in Figure 5a,b. The corresponding coordinates are provided as part of the Supporting Information and were also used to compute a model for the binding site of the $Fe(CN)_2CO$ fragment (Figure 2a). Strikingly, a primary docking site for ATP was calculated for *Ec*HypCD (Figure S19 and Tables S7 and S8) that was almost identical (including the Vina score) to that of *Tk*HypCD (Figure S20 and Tables S9 and S10). It is important to note, however, that ATP only docks in cavity A of *Ec*HypCD if the first three N-terminal amino acids Met-Cys-Ile of HypC (Met1 is cleaved by methionine aminopeptidase) were omitted from the docking calculations (Figure S19 and Table S8). These results are in line with the docking calculations performed on the experimentally determined coordinates of *Tk*HypCD (PDB: 3VYR), in which the position of Cys2 and Ile3 remained unresolved (Figure 3, Table S5). Consistently, docking calculations using an AlphaFold-predicted *Tk*HypCD complex, which contained the Cys2-Ile3 dipeptide, confirmed that ATP cannot dock to cavity A (Figure S20, Table S9). Based on these observations, we hypothesized that both the C-terminal part of HypC must be in the open conformation and the outermost N terminus of HypC must change its conformation to allow the binding of ATP in cavity A. In addition, the consistent AlphaFold 2 structure predictions and CB-Dock2 docking data for different HypCD scaffold complexes may allow conclusions to be drawn about HypC dynamics and its functioning.

Since the structural changes are restricted to a small part of the HypCD protein complex, we searched for an experimental method to detect such (dynamic) conformational changes. In recent years, crosslinking mass spectrometry (crosslinking MS) has emerged as key technology in structural biology for investigating protein conformations and protein−protein interactions.[39−42] Holo- and apo-*Ec*$HypC_S$-D preparations with or without ATP were treated with the UV-activatable crosslinker sulfo-SDA, which introduces specific distance constraints into proteins with an upper limit (Cα−Cα) between 25 and 30 Å, for subsequent crosslinked residue pairs (using a 1% link-level false discovery rate). The crosslinked protein samples were subjected to trypsin digestion, and the resulting (crosslinked) peptide mixtures were then analyzed using MS as described in the Methods section.

The crosslinking MS data obtained for holo-$HypC_S$-D (±ATP) are shown in Figure 6. Significantly, we indeed observed crosslinks indicating the existence of both an open and a closed conformation of the C-terminal part of HypC in the $HypC_S$-D complex. The crosslinks supporting that the C-terminal part of HypC is positioned in the closed conformation in holo-HypCD (−ATP) include that of residue K98, belonging to the Strep-tag II sequence located at the C terminus of HypC, with HypD residues Y363, Q368, and Y365 (Figure 6a, blue area) with an estimated distance of 22.5, 21.6, and 19.2 Å, respectively, according to the corresponding AlphaFold 2 model (Figure 6b, Table 1). In contrast, in the $HypC_S$-D model, where HypC is in the open conformation (Figure 6c), the estimated distances between the above-mentioned amino acid residues exceed the maximum expected length of 25−30 Å (Table 1) for chemical crosslinking.[43] Other diagnostic crosslinks are those between K98 of $HypC_S$ and the HypD residues Y122, S123, A131, N134, P135, and T136 (Figure 6a, yellow area). Here the distances span

https://doi.org/10.1021/jacs.4c09791
J. Am. Chem. Soc. 2024, 146, 30976−30989

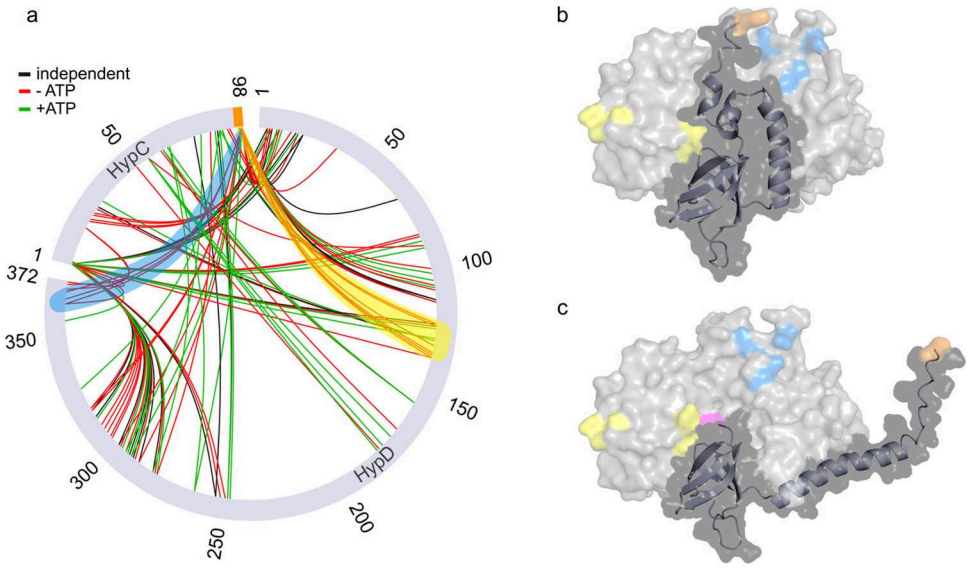

Figure 6. Crosslinking MS analysis of holo-HypC$_S$-D with and without ATP. (a) Circular view of the mass spectrometry analysis of the crosslinking within the holo-*Ec*HypC$_S$-D complex with or without ATP. HypC and HypD sequences are represented as gray, scaled bars and labeled accordingly. Amino acid numbering is given on the outside of the circle. Crosslinks between the two proteins are depicted as red (−ATP) and green (+ATP) lines. Crosslinks observed in both samples are depicted as black lines (independent). Crosslinks that support a closed conformation of the C-terminal part of HypC (panel b) are highlighted in transparent yellow and blue. The yellow area includes the residues K98 to Y122 as well as S123, A131, N134, P135, and T136, and the blue area includes the residues K98 to Y363 as well as Y365 and Q368. The distances between the amino acids of these crosslinks (aa to aa) were determined with PyMol and are listed in Table 1. Crosslinks in regions of the protein complex remote from the predicted ATP binding site are not discussed. Panels b and c show the AlphaFold 2-predicted *Ec*HypC−D structures in closed and open conformations, respectively, which contain the Strep-tag II peptide sequence at the C terminus of HypC. K98$_{HypC}$ is colored in orange and C2$_{HypC}$ in magenta. The colors of other highlighted residues correspond to the color code used in panel a. Note that C2$_{HypC}$ in the closed conformation is covered by the C-terminal part of HypC and therefore not visible.

Table 1. Amino Acid Distances of Selected Crosslinks in Holo-HypCD That Indicate an Open or a Closed Conformation of the C-Terminal Part of HypC

Cross-link (aa - aa)[a]	Distance (in Å) for **closed** conformation	Distance (in Å) for **open** conformation
K98 - Y363	20.8	47.6
K98 - Y365	16.3	51.1
K98 – Q368	17.5	46.3
K98 – Y122	26.3	62.0
K98 – S123	29.5	64.3
K98 – A 131	35.8	79.4
K98 – N134	34.4	79.5
K98 – P135	39.3	84.0
K98 – T136	38.9	85.6

[a]Blue and yellow colors correspond to those in Figure 6.

between 26 and 39 Å for the closed conformation and between 62 and 86 Å for the open conformation (Table 1).

Taking into account the flexibility of the Strep-tag II, which is not confidently predicted by the AlphaFold 2 model (Figure 6a and Figure S18) as well as the larger distances for K98 of HypC$_S$ and the residues of HypD in the open conformation that exceed the maximum distance for crosslinks, the MS data support the closed conformation of the C-terminal part of HypC$_S$ in holo-HypC$_S$-D (−ATP). Consistently, the above-mentioned crosslinks were not detected in the holo-HypC$_S$-D incubated with ATP, suggesting that the binding of the nucleotide causes the observed (and predicted) conformational changes in HypCD (Figure 6a). Moreover, the ATP-induced changes described above were not observed for apo-HypC$_S$-D (Figure S22), implying that the closed conformation of the C-terminal part is induced only in the absence of ATP when the protein is loaded with the Fe(CN)$_2$CO cofactor.

Our *in vitro* assays demonstrated that *Ec*HypCD utilizes ATP to deliver the Fe(CN)$_2$CO fragment to the apo-form of the hydrogenase large subunit. The combination of the AlphaFold 2 and crosslinking MS data indicates that this may occur through ATP-dependent conformational changes in HypCD, mainly at the C-terminal part of HypC, which suggests a competition-controlled mechanism of transfer for the Fe(CN)$_2$CO fragment. As ATP and the Fe(CN)$_2$CO fragment cannot bind simultaneously to the same protein pocket due to steric hindrance (both cofactors are predicted to be located at close distance from Cys41 in HypD), we propose that the binding of ATP triggers the dissociation of the Fe(CN)$_2$CO fragment from Cys41 in HypD. Consequently, the Fe(CN)$_2$CO synthon would remain bound to Cys2 of HypC. This scenario is consistent with a recent report by Gary Sawers' group showing that the HybG maturase (a HypC paralog) dissociated from HypD carries the Fe(CN)$_2$CO group, as evidenced by tandem MS/MS experiments.[16] HypC/HybG loaded with Fe(CN)$_2$CO would then deliver the iron fragment to the apo-form of the hydrogenase large subunit.

To structurally elucidate this interaction, we used AlphaFold 2 to compute a HypC−HoxC protein complex. The model predicts possible interactions between the two proteins, whereby Cys2 of HypC points toward the open cavity of the [NiFe]-binding site of HoxC (Figure S22). However, the low

https://doi.org/10.1021/jacs.4c09791
J. Am. Chem. Soc. 2024, 146, 30976−30989

predicted aligned error (PAE) values for the HypC−HoxC complex (Figure S18) indicate that the model is not highly reliable for the relative position of the two proteins to each other and, consequently, also for the position of the N terminus of HypC. By using the recently released AlphaFold 3 server, which allows structural predictions of protein complexes with nucleic acids, small molecules, and even metal ions,[44] a stable and highly reliable HypC−HoxC complex was predicted (Figure 7a and Figure S23 for PAE and pTM scores), in which the Cys2 of HypC protrudes into the [NiFe]-binding site of HoxC. Interestingly, the presence of an Fe ion in the active center (Figure 7b), which mimics the assembled $Fe(CN)_2CO$ fragment, induces a displacement of Cys482 of HoxC, which now strikingly adopts an arrangement reminiscent of the structure of the apo-large subunit HyhL from *T. kodakarensis* in complex with the Ni-chaperone HypA.[45] Importantly, both the HypCD (Figure S24) and HypCDE (Figure S25) complexes show no significant interactions with the large hydrogenase subunit according to the corresponding AlphaFold 2 models, which strengthens the hypothesis that the HypC protein alone delivers the Fe-$(CN)_2CO$ unit to the apo-form of the hydrogenase large subunit.

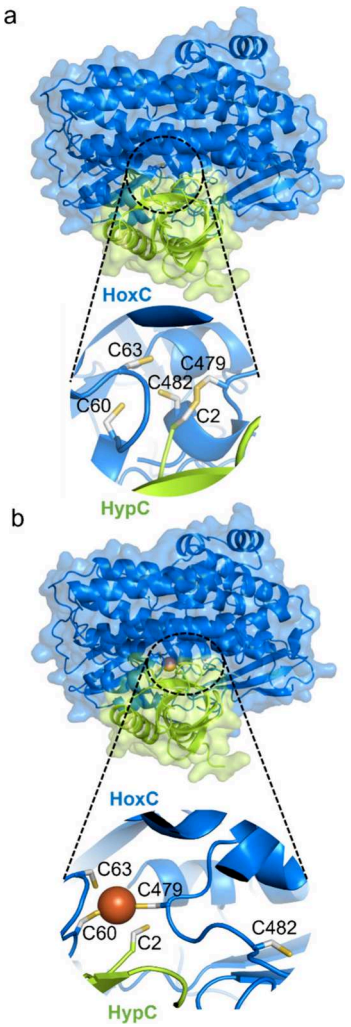

Figure 7. AlphaFold 3-predicted complexes between *Ec*HypC and *Cn*HoxC. (a) Cys2 of HypC protrudes into the [NiFe]-binding motif of HoxC, comprising the residues Cys60, 63, 479, and 482. (b) The predicted HypC−HoxC complex calculated in the presence of an Fe ion exhibits structural changes involving Cys482 of HoxC, which undergoes large displacements as compared to the predicted model in panel a. Note that Cys2 of HypC is still close to the [NiFe]-binding site. HoxC (blue) and HypC (green) are shown in surface and cartoon representations, and the [NiFe]-binding site of HoxC is shown in ball and stick representation with S in yellow, C in gray, and Fe in brown.

CONCLUSIONS

In this study, we investigated a key step in the assembly of the [NiFe]-hydrogenase active site, which is the HypCD-mediated incorporation of the low spin $Fe^{II}(CN)_2CO$ synthon into the apo-hydrogenase large subunit. Based on our biochemical, spectroscopic, and computational data, we draw the following conclusions about the role of the HypCD scaffold complex.

(1) Holo-HypCD houses two Fe-containing cofactors, a [4Fe−4S] cluster, and a low-spin Fe^{II} species with a 5-fold coordination comprising one CO, two CN^-, and two cysteine thiolates ($Cys2_{HypC}$ and $Cys41_{HypD}$, *E. coli* numbering) as ligands. (2) Binding of ATP, not its hydrolysis, is required for transfer of the $Fe(CN)_2CO$ moiety to the apo-form of the hydrogenase large subunit. Protein−ligand docking data identified an ATP binding site in a HypD cavity at the HypC−HypD interface. (3) The binding of ATP presumably takes place in the cavity that also accommodates the $Fe(CN)_2CO$ synthon, and among others, the synthon-binding Cys41 of HypD is involved in the ATP binding. Considering that Cys2 of HypC and Cys41 of HypD must be close to each other to stably bind the $Fe(CN)_2CO$ fragment,[32] we propose that the binding of ATP triggers significant rearrangements in HypCD, resulting in (i) the disruption of the $Fe(CN)_2CO$ thiolate complex with Cys41 of HypD and (ii) the displacement of the N-terminal Cys2 of HypC, which alone carries the $Fe(CN)_2CO$ fragment. As this step requires reducing power, the [4Fe−4S] cluster and the nearby thioredoxin (dithiol−disulfide) moiety represent possible electron donors.[22] (4) AlphaFold 2 structure predictions and crosslinking MS revealed significant ATP-dependent conformational changes of the C-terminal, mostly α-helical part of HypC exclusively in the holo-HypCD complex. An open and a closed conformation were identified that could reliably regulate the binding/dissociation of the ATP/$Fe(CN)_2CO$ cofactors, as depicted in Figure 8. (5) It has been hypothesized that the HypCD complex dissociates to allow the delivery of the $Fe(CN)_2CO$ fragment to the apo-form of the hydrogenase large subunit.[16] Our AlphaFold 3 data allow us to visualize a possible Fe-dependent interaction between the N terminus of HypC and the NiFe-binding site of the large subunit HoxC.

In summary, our results provide new insights into the sophisticated protein machinery responsible for [NiFe]-hydrogenase maturation. The fact that ATP and a non-hydrolyzable ATP analogue both trigger $Fe(CN)_2CO$ synthon transfer suggests that nucleotide binding alone induces the required structural rearrangements in the HypCD complex. This mechanism is reminiscent of previous observations on multidrug resistance protein MRP1,[46] RNA strand separation by DEAD-box proteins,[47] the proteasome-regulatory ATPase PAN,[48] clamp loading of DNA, which enhances the processivity of DNA polymerase,[49] and the molecular chaperone HSP90.[50] In all of these cases, ATP binding alone leads to structural changes important for initial functions, while ATP hydrolysis is required for later processes. In this sense, the

https://doi.org/10.1021/jacs.4c09791
J. Am. Chem. Soc. 2024, 146, 30976−30989

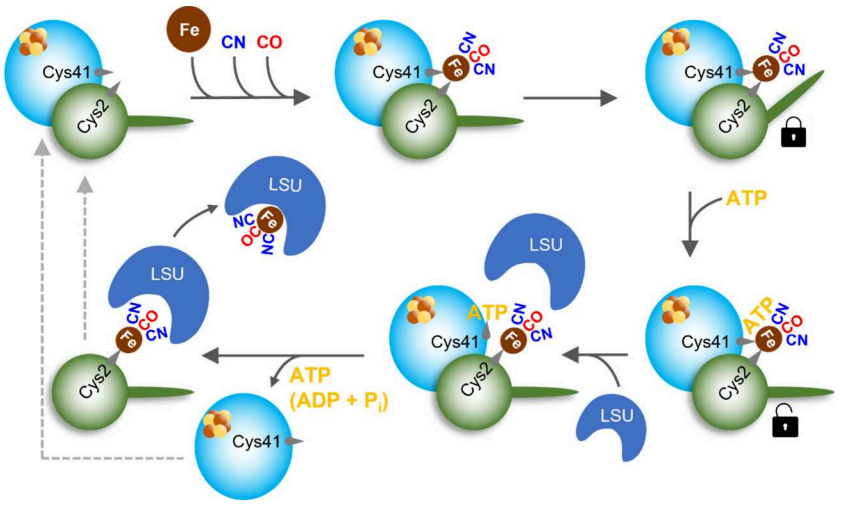

Figure 8. Scheme for the transfer of the $Fe(CN)_2CO$ fragment from HypCD to the apo-form of the hydrogenase large subunit. The [4Fe−4S] cluster-containing HypD protein is depicted in cyan, and HypC is in green. The C-terminal part of HypC remains in the open conformation until the $Fe(CN)_2CO$ synthon coordinated by $Cys41_{HypD}$ and $Cys2_{HypC}$ (numbering according to HypCD from *E. coli*) is fully assembled. Our data indicate that the C-terminal part of HypC in holo-HypCD adopts the closed conformation that protects the $Fe(CN)_2CO$ fragment until further use. Subsequent ATP binding first causes the HypC protein to adopt the open conformation and second, presumably in the presence of the large subunit (LSU), leads to the disruption of the S−$Fe(CN)_2CO$ bond with Cys41 of HypD and the concomitant rearrangement of the N-terminal Cys2 of HypC with the bound $Fe(CN)_2CO$ fragment. These structural changes are thought to destabilize the HypCD complex, thereby releasing ATP (or its hydrolysis products) and $Fe(CN)_2CO$-loaded HypC, which is then proposed to form a transient complex with LSU to deliver the $Fe(CN)_2CO$ fragment (Figure 7). The released HypC and HypD proteins can then enter another cycle (dashed lines).

ATP-hydrolyzing activity of HypCD might be important for the release of the nucleotide after synthon transfer, thereby priming the HypCD complex for another cycle (Figure 8). This could not be tested in our *in vitro* assay because it is inherently suitable for only a single transfer cycle. Therefore, we cannot exclude other roles for ATPase activity, e.g., in the synthesis or binding of the CN^- and CO ligands to the iron ion in HypCD. However, our results emphasize the importance of NTPases for the assembly of metallocofactors[51] and point to the essential role of ATP in the displacement of the $Fe(CN)_2CO$ synthon in the HypCD complex. This, in addition to the catalytic reactions of the maturases HypE and HypF,[6] is the third ATP-dependent function of [NiFe]-hydrogenase maturation.

METHODS

Bacterial Strains, Cultivation Conditions, and Protein Purification. For heterologous protein production, the *E. coli* strain Rosetta (DE3) was used. The corresponding expression plasmids are listed in Table S2, and their construction is described in Supplementary Methods (Table S11). Strains were grown aerobically in LB medium containing 100 μg/mL of carbenicillin and 34 μg/mL of chloramphenicol. Precultures were grown overnight at 37 °C and used to inoculate (1:100) 1 L main cultures, which were subsequently cultivated at 37 °C and 120 rpm until an OD_{600} between 0.4 and 0.8 was achieved. Gene expression was induced by adding 0.5 mM isopropyl beta-D-1-thiogalactopyranoside (IPTG). The cells were incubated overnight at 16 °C and 120 rpm and finally harvested by centrifugation at 11,500 × *g* for 15 min at 4 °C. Cell pellets were either processed immediately or frozen in liquid nitrogen and stored at −80 °C. All purification steps were performed aerobically at 4 °C. A 1 g sample of cell pellet was resuspended in 3 mL of the corresponding buffer (Table S1). Cell lysis was achieved in a French pressure cell with a pressure of 125 MPa. After ultracentrifugation at 100,000 × *g* for 45 min at 4 °C, the soluble extract was loaded onto either a Strep-Tactin Superflow resin (high-capacity, IBA Lifesciences) column or a HisPur Ni-NTA resin (Thermo Scientific) column, depending on the affinity tag. The washing and elution procedures as well as the buffer compositions are listed in Table S1. Eluted proteins were first concentrated (Ultracel Amicon Ultra 15 mL centrifugal filter units), followed by a 10-fold dilution with washing buffer, and then concentrated again by ultrafiltration. This process was repeated four times to wash away residual imidazole or D-desthiobiotin. Finally, protein aliquots were frozen and stored in liquid nitrogen. Concentration was determined via the Pierce BCA protein assay kit (Thermo Scientific).

Production of ^{57}Fe-labeled HypCD proteins was conducted as follows. When HypCD-overproducing cell cultures reached an OD_{600} between 0.4 and 0.8, 2.5 mL of $^{57}FeCl_2$ solution (20.5 mM in 1.5 M HCl) was added to achieve a final concentration of ca. 50 μM. Cells were first incubated for ∼20 min at room temperature (RT), and gene expression was then induced as described above. All purification steps were identical with those used to isolate HypCD from media containing iron with natural isotope distribution.

Polyacrylamide Gel Electrophoresis and Metal Determination. Protein purity was verified by SDS-PAGE. 3.5 μg of purified proteins was separated on a 15% acrylamide separating gel at 0.04 A for ca. 45 min. Protein bands were visualized by Coomassie staining. The metal content of the purified HypCD samples was determined via inductively coupled plasma optical emission spectrometry (ICP-OES). Three technical replicates of a 10 μM protein solution (each 500 μL) were mixed with 500 μL of nitric acid (65% v/v). After being incinerated at 100 °C overnight, samples were filled to 5 mL with ultrapure water and measured in an Optima 2100DV ICP-OES (PerkinElmer). The same procedure was repeated for three technical replicates of the buffer solution.

ATPase Activity of HypCD. ATPase activity was determined biochemically using a coupled enzymatic assay comprising a pyruvate kinase (PK) and a lactate dehydrogenase (LDH) from rabbit muscle (Sigma).[52] In a first reaction, ATP is hydrolyzed by HypCD to ADP and phosphate. The produced ADP and phosphoenolpyruvate (PEP) are then used by PK to form pyruvate and ATP. Last, pyruvate is consumed by LDH to form lactate. During this last assay reaction, NADH is oxidized to NAD^+, which is detected by UV−vis spectroscopy due to the decrease in absorbance at 340 nm (ε = 6.3 mM^{-1} cm^{-1}).[53] Each reaction was conducted at 25 °C in buffer containing 100 mM Tris/HCl, pH 7.5, 2.5 mM $MgCl_2$, 1 mM PEP, 1 mM ATP, and 0.3 mM NADH. The final amount of PK and LDH

https://doi.org/10.1021/jacs.4c09791
J. Am. Chem. Soc. 2024, 146, 30976−30989

was 4 and 3 U, respectively. To avoid an unspecific increase of absorbance due to residual ADP in the reaction mixture, HypCD was added when the absorbance of the solution reached a plateau. To verify that HypCD was exclusively responsible for ATP hydrolysis, we also recorded IR spectra of ATP with and without HypCD by monitoring the absorbances of the reactant and the hydrolysis products (Figure S13). In this case, HypCD was incubated in an anaerobic workstation with ATP, NaDT, and $MgCl_2$ in a molar excess of 40-fold, 30-fold, and 20-fold, respectively, and the mixture was then transferred to the IR cell.

Spectroscopy. *Infrared.* HypCD and HoxC protein solutions were transferred into a homemade, gastight, and temperature-controlled transmission cell equipped with two sandwiched CaF_2 windows separated by a Teflon spacer (optical path length of 50 μm). Spectra with a resolution of 2 cm^{-1} were recorded at 10 °C using a Bruker Tensor 27 Fourier-Transform spectrometer equipped with a liquid-nitrogen-cooled mercury cadmium telluride detector. The sample compartment was purged with dried air. For a single spectrum 200 individual scans were averaged. A buffer spectrum was used as a reference to calculate the corresponding absorbance spectra. OPUS software version 7.5 (Bruker) was used for data analysis.

Mössbauer. Zero-field Mössbauer spectra of ^{57}Fe-labeled HypCD apo- and holo-samples at a concentration of ca. 1.5 mM were acquired on a SEECO MS6 spectrometer comprising the following instruments: a JANIS CCS-850 cryostat, including a CTI-CRYOGENICS closed cycle 10 K refrigerator, and a CTI-CRYOGENICS 8200 helium compressor. The cold head and sample mount were equipped with calibrated DT-670-Cu-1.4L silicon diode temperature probes and heaters. The temperature was controlled by a LAKESHORE 335 temperature controller. Spectra were recorded using an LND-45431 Kr gas proportional counter with a beryllium window connected to the SEECO W204 γ-ray spectrometer that includes a high voltage supply, a 10 bit and 5 μs ADC, and two single channel analyzers. Motor control and recording of spectra were taken care of by the W304 resonant γ-ray spectrometer. For the reported spectra, a RIVERTEC MCO7.114 source (^{57}Co in Rh matrix) with an activity of about 1 GBq was used. All spectra were recorded on frozen solutions at 13 K, and data were accumulated for about 24−72 h. Mössbauer data were processed and simulated using the WMOSS4 program (www.wmoss.org). Isomeric shifts are referenced to α-iron at room temperature.

NRVS. NRVS measurements were conducted at a Petra III P01 (Germany) using 14.41 keV radiation (^{57}Fe). Raw NRVS data were converted to single-phonon ^{57}Fe partial vibrational densities of states (PVDOS) using the PHOENIX software package via the "NRVS Spectra Processing Tool" web interface (https://www.spectra.tools/). The energy scales were calibrated with a $[NEt_4][^{57}FeCl_4]$ sample characterized by two prominent peaks at 378 cm^{-1} (asymmetric Fe−Cl stretching mode) and 139 cm^{-1} (Fe−Cl bending mode).[54] The temperature of the samples was maintained at ca. 12 K by using a liquid He cryostat. The real sample temperature, as obtained from the spectral analysis, was 40−50 K. To enhance the signal-to-noise ratio in the Fe−CO/CN spectral range, sectional measurements were performed. Each scan was divided into two segments with different data collection times (second per point, s/pt). We used 3−4 s/pt for the region from −80 to 360 cm^{-1} and 9−10 s/pt for the region from 360 to 700 cm^{-1}.

UV−Visible. UV−vis spectra were recorded using a Cary50 UV−vis spectrophotometer (Varian, Agilent, USA) at room temperature. Each protein was used at a concentration of 40 μM. A buffer spectrum was used as a reference.

Crosslinking Mass Spectrometry. Apo-HypC_S-D was purified by affinity chromatography, while holo-HypC_S-D was additionally subjected to size-exclusion chromatography on a Superdex 200 Increase 10/300 GL (Cytiva) to remove unwanted oligomers (ternary HypCDE complex and HypC dimers). Purified HypCD complex (20 μg, 0.5 mg/mL) was crosslinked using sulfo-SDA (sulfosuccinimidyl 4,4′-azipentanoate (Thermo Scientific Pierce) at 0.76 mM in a crosslinking buffer (MOPS 50 mM, 150 mM NaCl, 0.1 mM DTT, pH 7.5). For the HypCD plus ATP sample, ATP was added to purified HypCD (9 mM final crosslinking reaction concentration) 10 min prior to addition of crosslinker. The crosslinking reaction involved two steps: 1. Crosslinker and protein were incubated for 30 min at room temperature in the dark; 2. The sample was irradiated with high-power UV light (LuxiGen 365 nm UV LED Gen 4 Emitter, LED Engine, operated at 1000 mA) for 20 s. After crosslinking, protein was acetone-precipitated and digested using an adapted SPEED protocol.[55] Briefly, pelleted proteins were dissolved in 10 μL of trifluoracetic acid (TFA), neutralized by addition of 100 μL of 2 M Tris base, and reduced and alkylated with the addition of 11 μL of TCEP/2-chloroacetamide (at final concentrations of 10 and 40 mM, respectively) and heating for 5 min at 95 °C. Protein samples were diluted 1:5 with water, and digestion was carried out for 20 h at 37 °C using trypsin at an enzyme:protein ratio of 1:50. Digests were acidified with TFA and desalted using C18 StageTips.[56]

LC-MS/MS analysis was performed on a Q Exactive High-Field (HF) Hybrid mass spectrometer (Thermo Fisher Scientific) coupled to an Ultimate 3000 UHPLC system (Dionex, Thermo Fisher Scientific). Peptides were separated on a 50 cm EASY-Spray column (Thermo Fisher). Mobile phase A consisted of 0.1% (v/v) formic acid and mobile phase B of 80% (v/v) acetonitrile with 0.1% (v/v) formic acid. The following LC gradient was applied with a flow rate of 300 nL/min: 2% B to 11% B in 10 min, to 35% B in 77 min, to 50% B in 5.5 min, ramping to 95% B in 2.5 min, and holding for 5 min (total run time, 120 min). Mass spec data were acquired in data-dependent mode, with both MS1 and MS2 scans carried out in the Orbitrap. Full scan mass spectra were recorded in the range of 400−1450 m/z at a resolution of 120,000 (AGC target, 1e6; injection time of 50 ms). The ten most intense ions in the full scan, with precursor charge states between 3+ and 6+, were isolated with a m/z window of 1.4 Th and fragmented using higher-energy collision-induced dissociation (HCD) at stepped normalized collision energies of 20, 28, and 30%. Subsequent fragmentation spectra were recorded at a resolution of 60,000, using an AGC target of 2e5 and maximum injection time set to 250 ms. Dynamic exclusion (single repeat count) was set to 30 s. Precursors m/z were recalibrated based on linear peptide identifications at <1% False Discovery Rate (FDR). Recalibrated peak lists were searched for crosslink identification against the sequences of HypC and HypD, using the Xi software suite (version 1.7.6.4; https://github.com/Rappsilber-Laboratory/xiSEARCH)[57] with the following settings: MS1 accuracy, 3 ppm; MS2 accuracy, 5 ppm; enzyme, trypsin, allowing up to 2 missed cleavages and 2 missing monoisotopic peaks; crosslinker, SDA (NHS-ester reaction specificity for lysine, serine, threonine, tyrosine, and protein N-termini); fixed modifications, carbamidomethylation on cysteine (cm, +57.02 Da); variable modifications, methylation on glutamic acid (me, +14.01), oxidation on methionine (ox, +15.99 Da), SDA-loop (+82.04 Da), and SDA-hyd (+100.05). SDA MS-cleavability was considered during the database search. Identified crosslinks were filtered to 1% FDR on link level with xiFDR version 2.2.RC2.[42]

3D Structure Predictions. The AlphaFold 2 models of HypCD complexes from *Thermococcus kodakarensis* (*Tk*) and *Escherichia coli* (*Ec*), the latter with and without the Strep-tag II sequence at the C terminus of HypC, as well as the complex between *Ec*HypC and HoxC from *C. necator* (*Cn*) were calculated using ColabFold v1.5.5.[58,59] For prediction of conformational variability, the following settings were applied: "max_msa" was set to "32:64", "num_seeds" was set to "16", and "use_dropouts" was not activated ("use_dropouts" did not lead to obvious structural changes when activated).[60] The accession numbers of the protein sequences used for the AlphaFold structure predictions (Supplementary Data I) are listed in Table 2. During preparation of the manuscript, AlphaFold 3 was released[44] and we used it to compute both the HypCD and HypC−HoxC complexes in the presence of ATP and Fe ions. The interatomic distances listed in Table 1 were determined using PyMOL 2.5.5.[61]

DFT Model Setup. Initial coordinates used for the density functional theory (DFT) modeling were constructed based on the (*i*) cofactor-free AlphaFold prediction of the *Ec*HypCD protein structure and (*ii*) $Fe(CN)_2(CO)(Cys)_2$ fragment extracted from the

https://doi.org/10.1021/jacs.4c09791
J. Am. Chem. Soc. 2024, 146, 30976−30989

Table 2. Accession Numbers of Protein Sequences Used for the AlphaFold Structure Predictions

Protein[a]	Accession number
*Tk*HypCD	3vyr (RCSB)
*Ec*HypC	P0AAM3 (UniProt)
*Ec*HypD	P24192 (UniProt)
*Cn*HoxC	Q79IP6 (UniProt)

[a]*Tk - Thermococcus kodakarensis, Ec - Escherichia coli, Cn - Cupriavidus necator.*

PDB 3RGW[62] (X-ray structure of the O_2-tolerant membrane-bound [NiFe]-hydrogenase from *Cupriavidus necator*). The $Fe(CN)_2(CO)$-$(Cys)_2$ fragment was docked manually into the *Ec*HypCD framework so that one of its cysteine side chains aligns with $Cys41_{HypD}$, and the second cysteine is positioned in the region of $Cys2_{HypC}$. Twelve more *Ec*HypCD residues in the environment of $Fe(CN)_2CO$ were retained in the DFT model as shown in Figure 2a and Figure S6, overall defining the system as $[\mathbf{C_2}]_{HypC} - Fe(CN)_2(CO) - [\mathbf{C_{41}}G_{42}G_{43}H_{44}/G_{68}C_{69}*/F_{147}/T_{149}/P_{199}G_{200}\mathbf{H_{201}}/F_{227}/\mathbf{E_{357}}]_{HypD}$ (metal ligands are in bold). Here, the backbone spacers were included between the consecutive HypD residues. The side chain of $Cys69_{HypD}$ (*) was omitted, equivalent to a C-to-G modification, as it points away from the cofactor. All the C_α carbon atoms were fixed to their reference AlphaFold positions during DFT structure optimization (see method details below) as often employed in protein modeling,[63] except that of $Cys2_{HypC}$, which varies its position (see the Results section). The titratable imidazole groups of $His44/201_{HypD}$ were singly protonated corresponding to the neutral pH. In contrast, $Glu357_{HypD}$ carboxylate was protonated due to its proximity to the $Cys2_{HypC}$ thiolate sulfur (Figure 2a and Figure S6).

DFT Methods. Molecular geometry optimization and subsequent Hessian were accomplished using Gaussian 16, revision C.01,[64] assisted with densities exported from single-point calculations using JAGUAR 11.0.[65] All calculations employed the PBE0[66] hybrid functional and the LACV3P** basis set as implemented in JAGUAR. For the first- and second-row elements, LACV3P** implies 6-311G** triple-ζ basis sets including polarization functions. For the Fe center, LACV3P** consists of a triple-ζ basis set for the outermost core and valence orbitals and the quasi-relativistic Los Alamos effective core potential (ECP) for the innermost electrons.[67,68] Molecular environment was considered using a self-consistent reaction field (SCRF) polarizable continuum model and integral equation formalism[69] (IEF-PCM) as implemented in Gaussian. The static dielectric constant was set to $\varepsilon = 4.0$, as often used for proteins, and the remaining IEF-PCM parameters were kept at their default values for water. The ^{57}Fe-PVDOS and interatomic relative displacement kinetic energy distribution (KED) intensities were extracted from Gaussian normal mode outputs using an in-house program Q-SPECTOR.[70] To empirically account for the observed NRVS line shape, the computed ^{57}Fe-PVDOS intensities were broadened by Lorentzian convolution with a full width at half-maximum (fwhm) of 14 cm^{-1}. For ^{57}Fe-PVDOS, empirical scaling by ×1.07/1.02/0.97 was applied to the calculated frequencies in the 400−560/560−610/610−660 cm^{-1} regions, respectively.

In Vitro Transfer Assay. All steps were carried out under anaerobic conditions in an anaerobic workstation with a temperature of about 10 °C. Buffer solutions and protein concentrators (Amicon Ultracel, Millipore, 30 kDa cutoff) were degassed prior to usage and equilibrated with anaerobic buffer. The assay was carried out in a 1.5 mL Eppendorf vial with the following components: 50 mM MOPS/KOH, pH 7.4 at 4 °C, 150 mM NaCl, 15 mM NaDT, 10 mM $MgCl_2$, 20 mM of ATP/GTP/non-hydrolyzable ATP analogue (see Table S6 for further details). 0.06 mM apo-$HoxC_S$ (0.06 mM) was reacted with 0.3 mM holo-$HypC_H$-D protein solution (5 mol equiv). After incubation, the whole assay reaction was loaded on a Strep-Tactin Superflow column (high-capacity, iba Lifescience) with a column volume (CV) of 1 mL, to isolate $HoxC_{strep}$ from the reaction mixture. The column was washed with 10 CVs of washing buffer (50 mM MOPS/KOH, pH 7.4 at 4 °C, 150 mM NaCl), and the matrix-bound protein was eluted with 5 CVs of washing buffer supplemented with 3.0 mM D-desthiobiotin. Elution fractions were concentrated using Ultracel Amicon Ultra 0.5 mL centrifugal filter units (cutoff 30 kDa) followed by a 5-fold dilution step with washing buffer to remove residual desthiobiotin. The washing step was repeated 4 times, followed by a final step of protein concentration (resulting volume of ca. 20 μL) and IR measurements.

CB-Dock2 Cavity Detection-Guided Blind Docking. For a protein−ligand blind docking simulation the online tool CB-Dock2 was used.[34,35] The X-rays coordinates of *T. kodakarensis* HypCD[32] and the AlphaFold-predicted structures of *E. coli* HypCD (Supplementary Data I) were employed as proteins. As ligand, the coordinates of ATP (DrugBank ID: DB00171) were used. The docking simulation is based on a perl script that processes the submitted files as described at https://cadd.labshare.cn/cb-dock2/php/manual.php. AutoDock-Vina (version 1.2.0) is used for template-independent blind docking, and template-based blind docking uses the BioLip database (version 2021.09.15) as the template database. Output files are given as receptor−ligand PDB files for all detected cavities (Supplementary Data II).

■ ASSOCIATED CONTENT

Data Availability Statement

The authors declare that the data supporting the findings of this study are available within the article and the Supporting Information. Raw NRVS data were generated at the synchrotron facility Petra III, and are available in their processed form upon request. Crosslinking MS data are deposited to the ProteomeXchange Consortium via the PRIDE database with the data set identifier PXD051661 and 10.6019/PXD051661.

Supporting Information

The Supporting Information is available free of charge at https://pubs.acs.org/doi/10.1021/jacs.4c09791.

Supplementary Figures S1−S25, supplementary Tables S1−S11, supplementary note on ATPase activity measurements, supplementary methods, and supplementary references (PDF)

AlphaFold structure predictions (Supplementary Data I), output files of CB-Dock2 (Supplementary Data II), and selected DFT normal mode animations (GIF format) relevant to NRVS bands and the optimized structures (PDB format) for the DFT-computed models (Supplementary Data III) (ZIP)

■ AUTHOR INFORMATION

Corresponding Authors

Giorgio Caserta − *Institut für Chemie, Technische Universität Berlin, 10623 Berlin, Germany;* orcid.org/0000-0003-0986-3059; Email: giorgio.caserta@tu-berlin.de

Oliver Lenz − *Institut für Chemie, Technische Universität Berlin, 10623 Berlin, Germany;* orcid.org/0000-0003-4550-5128; Email: oliver.lenz@tu-berlin.de

Authors

Anna Kwiatkowski − *Institut für Chemie, Technische Universität Berlin, 10623 Berlin, Germany*

Anne-Christine Schulz − *Institut für Chemie, Technische Universität Berlin, 10623 Berlin, Germany*

Stefan Frielingsdorf − *Institut für Chemie, Technische Universität Berlin, 10623 Berlin, Germany;* orcid.org/0000-0002-4141-7836

Vladimir Pelmenschikov − *Institut für Chemie, Technische Universität Berlin, 10623 Berlin, Germany;* orcid.org/0000-0002-0523-4418
Kilian Weisser − *Institute of Chemistry, Humboldt-Universität zu Berlin, 12489 Berlin, Germany*
Adam Belsom − *Institute of Biotechnology, Chair of Bioanalytics, Technische Universität Berlin, 13355 Berlin, Germany;* orcid.org/0000-0002-8442-4964
Juri Rappsilber − *Institute of Biotechnology, Chair of Bioanalytics, Technische Universität Berlin, 13355 Berlin, Germany; Si-M/'Der Simulierte Mensch', a Science Framework of Technische Universität Berlin and Charité − Universitätsmedizin Berlin, 10623 Berlin, Germany; Wellcome Centre of Cell Biology, University of Edinburgh, Edinburgh EH9 3BF, U.K.*
Ilya Sergueev − *Deutsches Elektronen-Synchrotron, 22607 Hamburg, Germany*
Christian Limberg − *Institute of Chemistry, Humboldt-Universität zu Berlin, 12489 Berlin, Germany;* orcid.org/0000-0002-0751-1386
Maria-Andrea Mroginski − *Institut für Chemie, Technische Universität Berlin, 10623 Berlin, Germany;* orcid.org/0000-0002-7497-5631
Ingo Zebger − *Institut für Chemie, Technische Universität Berlin, 10623 Berlin, Germany;* orcid.org/0000-0002-6354-3585

Complete contact information is available at: https://pubs.acs.org/10.1021/jacs.4c09791

Notes

The authors declare no competing financial interest.

■ ACKNOWLEDGMENTS

This work was supported by the Deutsche Forschungsgemeinschaft (DFG, German Research Foundation) through the SPP 1927 "Iron Sulfur for Life" project no. 311062227 (O.L., I.Z., A.K.), project 449713269 (A.B.), and the cluster of excellence "UniSysCat" under Germany's Excellence Strategy-EXC2008-390540038. G.C., V.P., M.-A.M., and O.L. thank the COST Action FeSImmChemNet, CA21115, supported by COST (European Cooperation in Science and Technology). The Wellcome Centre for Cell Biology is supported by core funding from the Wellcome Trust [203149] (J.R.). We acknowledge DESY (Hamburg, Germany), a member of the Helmholtz Association HGF, for the provision of experimental facilities. Parts of this research were carried out at Petra III. Beamtime was allocated for proposals I-20220851 and I-20210325. We thank Silke Leimkühler and co-workers (Universität Potsdam) for ICP-OES measurements.

■ ABBREVIATIONS

DFT, density functional theory; IR, infrared; NRVS, nuclear resonance vibrational spectroscopy; PVDOS, partial vibrational densities of states; UV−vis, ultraviolet/visible

■ REFERENCES

(1) Lubitz, W.; Ogata, H.; Rüdiger, O.; Reijerse, E. Hydrogenases. *Chem. Rev.* **2014**, *114*, 4081−4148.
(2) Jones, A. K.; Lenz, O.; Strack, A.; Buhrke, T.; Friedrich, B. NiFe Hydrogenase Active Site Biosynthesis: Identification of Hyp Protein Complexes in *Ralstonia eutropha*. *Biochemistry* **2004**, *43*, 13467−13477.
(3) Böck, A.; King, P. W.; Blokesch, M.; Posewitz, M. C. Maturation of Hydrogenases. *Adv. Microb. Physiol.* **2006**, *51*, 1−71.
(4) Lacasse, M. J.; Zamble, D. B. [NiFe]-Hydrogenase Maturation. *Biochemistry* **2016**, *55*, 1689−1701.
(5) Watanabe, S.; Sasaki, D.; Tominaga, T.; Miki, K. Structural Basis of [NiFe] Hydrogenase Maturation by Hyp Proteins. *Biol. Chem.* **2012**, *393*, 1089−1100.
(6) Reissmann, S.; Hochleitner, E.; Wang, H.; Paschos, A.; Lottspeich, F.; Glass, R. S.; Böck, A. Taming of a Poison: Biosynthesis of the NiFe-Hydrogenase Cyanide Ligands. *Science* **2003**, *299*, 1067−1070.
(7) Bürstel, I.; Siebert, E.; Frielingsdorf, S.; Zebger, I.; Friedrich, B.; Lenz, O. CO Synthesized from the Central One-Carbon Pool as Source for the Iron Carbonyl in O_2-Tolerant [NiFe]-Hydrogenase. *Proc. Natl. Acad. Sci. U.S.A.* **2016**, *113*, 14722−14726.
(8) Schulz, A.-C.; Frielingsdorf, S.; Pommerening, P.; Lauterbach, L.; Bistoni, G.; Neese, F.; Oestreich, M.; Lenz, O. Formyltetrahydrofolate Decarbonylase Synthesizes the Active Site CO Ligand of O_2-Tolerant [NiFe] Hydrogenase. *J. Am. Chem. Soc.* **2020**, *142*, 1457−1464.
(9) Bürstel, I.; Hummel, P.; Siebert, E.; Wisitruangsakul, N.; Zebger, I.; Friedrich, B.; Lenz, O. Probing the Origin of the Metabolic Precursor of the CO Ligand in the Catalytic Center of [NiFe] Hydrogenase. *J. Biol. Chem.* **2011**, *286*, 44937−44944.
(10) Soboh, B.; Stripp, S. T.; Bielak, C.; Lindenstrauß, U.; Braussemann, M.; Javaid, M.; Hallensleben, M.; Granich, C.; Herzberg, M.; Heberle, J.; Sawers, R. G. The [NiFe]-hydrogenase Accessory Chaperones HypC and HybG of *Escherichia coli* Are Iron- and Carbon Dioxide-binding Proteins. *FEBS Lett.* **2013**, *587*, 2512−2516.
(11) Lacasse, M. J.; Douglas, C. D.; Zamble, D. B. Mechanism of Selective Nickel Transfer from HypB to HypA, *Escherichia coli* [NiFe]-Hydrogenase Accessory Proteins. *Biochemistry* **2016**, *55*, 6821−6831.
(12) Pinske, C.; Thomas, C.; Nutschan, K.; Sawers, R. G. Delimiting the Function of the C-Terminal Extension of the *Escherichia coli* [NiFe]-Hydrogenase 2 Large Subunit Precursor. *Front. Microbiol.* **2019**, *10*, 2223.
(13) Senger, M.; Stripp, S. T.; Soboh, B. Proteolytic Cleavage Orchestrates Cofactor Insertion and Protein Assembly in [NiFe]-Hydrogenase Biosynthesis. *J. Biol. Chem.* **2017**, *292*, 11670−11681.
(14) Hartmann, S.; Frielingsdorf, S.; Caserta, G.; Lenz, O. A Membrane-bound [NiFe]-Hydrogenase Large Subunit Precursor Whose C-Terminal Extension Is Not Essential for Cofactor Incorporation but Guarantees Optimal Maturation. *MicrobiologyOpen* **2020**, *9*, 1197−1206.
(15) Caserta, G.; Hartmann, S.; Van Stappen, C.; Karafoulidi-Retsou, C.; Lorent, C.; Yelin, S.; Keck, M.; Schoknecht, J.; Sergueev, I.; Yoda, Y.; Hildebrandt, P.; Limberg, C.; DeBeer, S.; Zebger, I.; Frielingsdorf, S.; Lenz, O. Stepwise Assembly of the Active Site of [NiFe]-Hydrogenase. *Nat. Chem. Biol.* **2023**, *19*, 498−506.
(16) Arlt, C.; Nutschan, K.; Haase, A.; Ihling, C.; Tänzler, D.; Sinz, A.; Sawers, R. G. Native Mass Spectrometry Identifies the HybG Chaperone as Carrier of the $Fe(CN)_2CO$ Group during Maturation of *E. coli* [NiFe]-Hydrogenase 2. *Sci. Rep* **2021**, *11*, 24362.
(17) Nutschan, K.; Golbik, R. P.; Sawers, R. G. The Iron-Sulfur-containing HypC-HypD Scaffold Complex of the [NiFe]-hydrogenase Maturation Machinery Is an ATPase. *FEBS Open Bio* **2019**, *9*, 2072−2079.
(18) Haase, A.; Sawers, R. G. A Redox-active HybG-HypD Scaffold Complex Is Required for Optimal ATPase Activity during [NiFe]-hydrogenase Maturation in *Escherichia coli*. *FEBS Open Bio* **2023**, *13* (2), 341−351.
(19) Blokesch, M.; Albracht, S. P. J.; Matzanke, B. F.; Drapal, N. M.; Jacobi, A.; Böck, A. The Complex Between Hydrogenase-Maturation Proteins HypC and HypD Is an Intermediate in the Supply of Cyanide to the Active Site Iron of [NiFe]-Hydrogenases. *J. Mol. Biol.* **2004**, *344*, 155−167.
(20) Bürstel, I.; Siebert, E.; Winter, G.; Hummel, P.; Zebger, I.; Friedrich, B.; Lenz, O. A Universal Scaffold for Synthesis of the

Fe(CN)$_2$(CO) Moiety of [NiFe] Hydrogenase. *J. Biol. Chem.* **2012**, *287*, 38845−38853.
(21) Soboh, B.; Stripp, S. T.; Muhr, E.; Granich, C.; Braussemann, M.; Herzberg, M.; Heberle, J.; Gary Sawers, R. [NiFe]-hydrogenase Maturation: Isolation of a HypC-HypD Complex Carrying Diatomic CO and CN^- Ligands. *FEBS Lett.* **2012**, *586*, 3882−3887.
(22) Stripp, S. T.; Oltmanns, J.; Müller, C. S.; Ehrenberg, D.; Schlesinger, R.; Heberle, J.; Adrian, L.; Schünemann, V.; Pierik, A. J.; Soboh, B. Electron Inventory of the Iron-Sulfur Scaffold Complex HypCD Essential in [NiFe]-Hydrogenase Cofactor Assembly. *Biochem. J.* **2021**, *478*, 3281−3295.
(23) Haase, A.; Arlt, C.; Sinz, A.; Sawers, R. G. Evidence the Isc Iron-Sulfur Cluster Biogenesis Machinery Is the Source of Iron for [NiFe]-Cofactor Biosynthesis in *Escherichia coli*. *Sci. Rep.* **2024**, *14*, 3026.
(24) Pandelia, M.-E.; Lanz, N. D.; Booker, S. J.; Krebs, C. Mössbauer Spectroscopy of Fe/S Proteins. *Biochim. Biophys. Acta* **2015**, *1853*, 1395−1405.
(25) Roncaroli, F.; Bill, E.; Friedrich, B.; Lenz, O.; Lubitz, W.; Pandelia, M.-E. Cofactor Composition and Function of a H_2-Sensing Regulatory Hydrogenase as Revealed by Mössbauer and EPR Spectroscopy. *Chem. Sci.* **2015**, *6*, 4495−4507.
(26) Caserta, G.; Lorent, C.; Pelmenschikov, V.; Schoknecht, J.; Yoda, Y.; Hildebrandt, P.; Cramer, S. P.; Zebger, I.; Lenz, O. *In Vitro* Assembly as a Tool to Investigate Catalytic Intermediates of [NiFe]-Hydrogenase. *ACS Catal.* **2020**, *10*, 13890−13894.
(27) Kamali, S.; Wang, H.; Mitra, D.; Ogata, H.; Lubitz, W.; Manor, B. C.; Rauchfuss, T. B.; Byrne, D.; Bonnefoy, V.; Jenney, F. E.; Adams, M. W. W.; Yoda, Y.; Alp, E.; Zhao, J.; Cramer, S. P. Observation of the Fe-CN and Fe-CO Vibrations in the Active Site of [NiFe] Hydrogenase by Nuclear Resonance Vibrational Spectroscopy. *Angew. Chem., Int. Ed.* **2013**, *52*, 724−728.
(28) Ogata, H.; Krämer, T.; Wang, H.; Schilter, D.; Pelmenschikov, V.; Van Gastel, M.; Neese, F.; Rauchfuss, T. B.; Gee, L. B.; Scott, A. D.; Yoda, Y.; Tanaka, Y.; Lubitz, W.; Cramer, S. P. Hydride Bridge in [NiFe]-Hydrogenase Observed by Nuclear Resonance Vibrational Spectroscopy. *Nat. Commun.* **2015**, *6*, 7890.
(29) Caserta, G.; Pelmenschikov, V.; Lorent, C.; Tadjoung Waffo, A. F.; Katz, S.; Lauterbach, L.; Schoknecht, J.; Wang, H.; Yoda, Y.; Tamasaku, K.; Kaupp, M.; Hildebrandt, P.; Lenz, O.; Cramer, S. P.; Zebger, I. Hydroxy-Bridged Resting States of a [NiFe]-Hydrogenase Unraveled by Cryogenic Vibrational Spectroscopy and DFT Computations. *Chem. Sci.* **2021**, *12*, 2189−2197.
(30) Lauterbach, L.; Gee, L. B.; Pelmenschikov, V.; Jenney, F. E.; Kamali, S.; Yoda, Y.; Adams, M. W. W.; Cramer, S. P. Characterization of the $[3Fe\text{-}4S]^{0/1+}$ Cluster from the D14C Variant of *Pyrococcus furiosus* Ferredoxin via Combined NRVS and DFT Analyses. *Dalton Trans.* **2016**, *45*, 7215−7219.
(31) Albareda, M.; Palacios, J.-M.; Imperial, J.; Pacios, L. F. Computational Study of the Fe(CN)$_2$CO Cofactor and Its Binding to HypC Protein. *J. Phys. Chem. B* **2013**, *117*, 13523−13533.
(32) Watanabe, S.; Matsumi, R.; Atomi, H.; Imanaka, T.; Miki, K. Crystal Structures of the HypCD Complex and the HypCDE Ternary Complex: Transient Intermediate Complexes during [NiFe] Hydrogenase Maturation. *Structure* **2012**, *20*, 2124−2137.
(33) Blokesch, M.; Böck, A. Properties of the [NiFe]-Hydrogenase Maturation Protein HypD. *FEBS Lett.* **2006**, *580*, 4065−4068.
(34) Yang, X.; Liu, Y.; Gan, J.; Xiao, Z.-X.; Cao, Y. FitDock: Protein-Ligand Docking by Template Fitting. *Brief. Bioinform.* **2022**, *23*, bbac087.
(35) Liu, Y.; Yang, X.; Gan, J.; Chen, S.; Xiao, Z.-X.; Cao, Y. CB-Dock2: Improved Protein-Ligand Blind Docking by Integrating Cavity Detection, Docking and Homologous Template Fitting. *Nucleic Acids Res.* **2022**, *50*, W159−W164.
(36) Tominaga, T.; Watanabe, S.; Matsumi, R.; Atomi, H.; Imanaka, T.; Miki, K. Crystal Structures of the Carbamoylated and Cyanated Forms of HypE for [NiFe] Hydrogenase Maturation. *Proc. Natl. Acad. Sci. U.S.A.* **2013**, *110*, 20485−20490.
(37) Watanabe, S.; Matsumi, R.; Arai, T.; Atomi, H.; Imanaka, T.; Miki, K. Crystal Structures of [NiFe] Hydrogenase Maturation Proteins HypC, HypD, and HypE: Insights into Cyanation Reaction by Thiol Redox Signaling. *Mol. Cell* **2007**, *27*, 29−40.
(38) Stripp, S. T.; Soboh, B.; Lindenstrauss, U.; Braussemann, M.; Herzberg, M.; Nies, D. H.; Sawers, R. G.; Heberle, J. HypD Is the Scaffold Protein for Fe-(CN)$_2$CO Cofactor Assembly in [NiFe]-Hydrogenase Maturation. *Biochemistry* **2013**, *52*, 3289−3296.
(39) Piersimoni, L.; Kastritis, P. L.; Arlt, C.; Sinz, A. Cross-Linking Mass Spectrometry for Investigating Protein Conformations and Protein-Protein Interactions—A Method for All Seasons. *Chem. Rev.* **2022**, *122*, 7500−7531.
(40) Schneider, M.; Belsom, A.; Rappsilber, J. Protein Tertiary Structure by Crosslinking/Mass Spectrometry. *Trends Biochem. Sci.* **2018**, *43*, 157−169.
(41) Leitner, A.; Bonvin, A. M. J. J.; Borchers, C. H.; Chalkley, R. J.; Chamot-Rooke, J.; Combe, C. W.; Cox, J.; Dong, M.-Q.; Fischer, L.; Götze, M.; Gozzo, F. C.; Heck, A. J. R.; Hoopmann, M. R.; Huang, L.; Ishihama, Y.; Jones, A. R.; Kalisman, N.; Kohlbacher, O.; Mechtler, K.; Moritz, R. L.; Netz, E.; Novak, P.; Petrotchenko, E.; Sali, A.; Scheltema, R. A.; Schmidt, C.; Schriemer, D.; Sinz, A.; Sobott, F.; Stengel, F.; Thalassinos, K.; Urlaub, H.; Viner, R.; Vizcaíno, J. A.; Wilkins, M. R.; Rappsilber, J. Toward Increased Reliability, Transparency, and Accessibility in Cross-Linking Mass Spectrometry. *Structure* **2020**, *28*, 1259−1268.
(42) Lenz, S.; Sinn, L. R.; O'Reilly, F. J.; Fischer, L.; Wegner, F.; Rappsilber, J. Reliable Identification of Protein-Protein Interactions by Crosslinking Mass Spectrometry. *Nat. Commun.* **2021**, *12*, 3564.
(43) Merkley, E. D.; Rysavy, S.; Kahraman, A.; Hafen, R. P.; Daggett, V.; Adkins, J. N. Distance Restraints from Crosslinking Mass Spectrometry: Mining a Molecular Dynamics Simulation Database to Evaluate Lysine-Lysine Distances. *Protein Sci.* **2014**, *23*, 747−759.
(44) Abramson, J.; Adler, J.; Dunger, J.; Evans, R.; Green, T.; Pritzel, A.; Ronneberger, O.; Willmore, L.; Ballard, A. J.; Bambrick, J.; Bodenstein, S. W.; Evans, D. A.; Hung, C.-C.; O'Neill, M.; Reiman, D.; Tunyasuvunakool, K.; Wu, Z.; Žemgulytė, A.; Arvaniti, E.; Beattie, C.; Bertolli, O.; Bridgland, A.; Cherepanov, A.; Congreve, M.; Cowen-Rivers, A. I.; Cowie, A.; Figurnov, M.; Fuchs, F. B.; Gladman, H.; Jain, R.; Khan, Y. A.; Low, C. M. R.; Perlin, K.; Potapenko, A.; Savy, P.; Singh, S.; Stecula, A.; Thillaisundaram, A.; Tong, C.; Yakneen, S.; Zhong, E. D.; Zielinski, M.; Žídek, A.; Bapst, V.; Kohli, P.; Jaderberg, M.; Hassabis, D.; Jumper, J. M. Accurate Structure Prediction of Biomolecular Interactions with AlphaFold 3. *Nature* **2024**, *630*, 493−500.
(45) Kwon, S.; Watanabe, S.; Nishitani, Y.; Kawashima, T.; Kanai, T.; Atomi, H.; Miki, K. Crystal Structures of a [NiFe] Hydrogenase Large Subunit HyhL in an Immature State in Complex with a Ni Chaperone HypA. *Proc. Natl. Acad. Sci. U.S.A.* **2018**, *115*, 7045−7050.
(46) Johnson, Z. L.; Chen, J. ATP Binding Enables Substrate Release from Multidrug Resistance Protein 1. *Cell* **2018**, *172*, 81−89.
(47) Liu, F.; Putnam, A.; Jankowsky, E. ATP Hydrolysis Is Required for DEAD-Box Protein Recycling but Not for Duplex Unwinding. *Proc. Natl. Acad. Sci. U.S.A.* **2008**, *105*, 20209−20214.
(48) Smith, D. M.; Kafri, G.; Cheng, Y.; Ng, D.; Walz, T.; Goldberg, A. L. ATP Binding to PAN or the 26S ATPases Causes Association with the 20S Proteasome, Gate Opening, and Translocation of Unfolded Proteins. *Mol. Cell* **2005**, *20*, 687−698.
(49) Yao, N. Y.; O'Donnell, M. The RFC Clamp Loader: Structure and Function. In *The Eukaryotic Replisome: a Guide to Protein Structure and Function*; MacNeill, S., Ed.; Subcellular Biochemistry; Springer: Dordrecht, The Netherlands, 2012; Vol. *62*, pp 259−279.
(50) Pearl, L. H. Review: The HSP90 Molecular Chaperone—an Enigmatic ATPase. *Biopolymers* **2016**, *105*, 594−607.
(51) Vaccaro, F. A.; Drennan, C. L. The Role of Nucleoside Triphosphate Hydrolase Metallochaperones in Making Metalloenzymes. *Metallomics* **2022**, *14*, mfac030.
(52) Kornberg, A.; Pricer, W. E. Enzymatic phosphorylation of adenosine and 2,6-diaminopurine riboside. *J. Biol. Chem.* **1951**, *193*, 481−495.

https://doi.org/10.1021/jacs.4c09791
J. Am. Chem. Soc. 2024, 146, 30976−30989

(53) Bergmeyer, H. U. Neue Werte für die molaren Extinktions-Koeffizienten von NADH und NADPH zum Gebrauch im Routine-Laboratorium. *Z. Klein. Chem. Klein. Biochem.* **1975**, *13*, 507−508.
(54) Gee, L. B.; Wang, H.; Cramer, S. P. NRVS for Fe in Biology: Experiment and Basic Interpretation. *Methods Enzymol.* **2018**, *599*, 409−425.
(55) Doellinger, J.; Schneider, A.; Hoeller, M.; Lasch, P. Sample Preparation by Easy Extraction and Digestion (SPEED) - A Universal, Rapid, and Detergent-Free Protocol for Proteomics Based on Acid Extraction. *Mol. Cell. Proteomics* **2020**, *19*, 209−222.
(56) Rappsilber, J.; Mann, M.; Ishihama, Y. Protocol for Micro-Purification, Enrichment, Pre-Fractionation and Storage of Peptides for Proteomics Using StageTips. *Nat. Protoc.* **2007**, *2*, 1896−1906.
(57) Mendes, M. L.; Fischer, L.; Chen, Z. A.; Barbon, M.; O'Reilly, F. J.; Giese, S. H.; Bohlke-Schneider, M.; Belsom, A.; Dau, T.; Combe, C. W.; Graham, M.; Eisele, M. R.; Baumeister, W.; Speck, C.; Rappsilber, J. An Integrated Workflow for Crosslinking Mass Spectrometry. *Mol. Syst. Biol.* **2019**, *15*, No. e8994.
(58) Mirdita, M.; Schütze, K.; Moriwaki, Y.; Heo, L.; Ovchinnikov, S.; Steinegger, M. ColabFold: Making Protein Folding Accessible to All. *Nat. Methods* **2022**, *19*, 679−682.
(59) Jumper, J.; Evans, R.; Pritzel, A.; Green, T.; Figurnov, M.; Ronneberger, O.; Tunyasuvunakool, K.; Bates, R.; Žídek, A.; Potapenko, A.; Bridgland, A.; Meyer, C.; Kohl, S. A. A.; Ballard, A. J.; Cowie, A.; Romera-Paredes, B.; Nikolov, S.; Jain, R.; Adler, J.; Back, T.; Petersen, S.; Reiman, D.; Clancy, E.; Zielinski, M.; Steinegger, M.; Pacholska, M.; Berghammer, T.; Bodenstein, S.; Silver, D.; Vinyals, O.; Senior, A. W.; Kavukcuoglu, K.; Kohli, P.; Hassabis, D. Highly Accurate Protein Structure Prediction with AlphaFold. *Nature* **2021**, *596*, 583−589.
(60) Kim, G.; Lee, S.; Karin, E. L.; Kim, H.; Moriwaki, Y.; Ovchinnikov, S.; Steinegger, M.; Mirdita, M. Easy and Accurate Protein Structure Prediction Using ColabFold. *Res. Sq.* **2023**, DOI: 10.21203/rs.3.pex-2490/v1.
(61) Schroedinger, LLC. *The PyMOL Molecular Graphics System*, version 2.5.5.
(62) Fritsch, J.; Scheerer, P.; Frielingsdorf, S.; Kroschinsky, S.; Friedrich, B.; Lenz, O.; Spahn, C. M. T. The Crystal Structure of an Oxygen-Tolerant Hydrogenase Uncovers a Novel Iron-Sulphur Centre. *Nature* **2011**, *479*, 249−252.
(63) Pelmenschikov, V.; Blomberg, M. R.; Siegbahn, P. E. A Theoretical Study of the Mechanism for Peptide Hydrolysis by Thermolysin. *J. Biol. Inorg. Chem.* **2002**, *7* (3), 284−298.
(64) Frisch, M. J.; Trucks, G. W.; Schlegel, H. B.; Scuseria, G. E.; Robb, M. A.; Cheeseman, J. R.; Scalmani, G.; Barone, V.; Petersson, G. A.; Nakatsuji, H.; Li, X.; Caricato, M.; Marenich, A. V.; Bloino, J.; Janesko, B. G.; Gomperts, R.; Mennucci, B.; Hratchian, H. P.; Ortiz, J. V.; Izmaylov, A. F.; Sonnenberg, J. L.; Williams; Ding, F.; Lipparini, F.; Egidi, F.; Goings, J.; Peng, B.; Petrone, A.; Henderson, T.; Ranasinghe, D.; Zakrzewski, V. G.; Gao, J.; Rega, N.; Zheng, G.; Liang, W.; Hada, M.; Ehara, M.; Toyota, K.; Fukuda, R.; Hasegawa, J.; Ishida, M.; Nakajima, T.; Honda, Y.; Kitao, O.; Nakai, H.; Vreven, T.; Throssell, K.; Montgomery, J. A., Jr.; Peralta, J. E.; Ogliaro, F.; Bearpark, M. J.; Heyd, J. J.; Brothers, E. N.; Kudin, K. N.; Staroverov, V. N.; Keith, T. A.; Kobayashi, R.; Normand, J.; Raghavachari, K.; Rendell, A. P.; Burant, J. C.; Iyengar, S. S.; Tomasi, J.; Cossi, M.; Millam, J. M.; Klene, M.; Adamo, C.; Cammi, R.; Ochterski, J. W.; Martin, R. L.; Morokuma, K.; Farkas, O.; Foresman, J. B.; Fox, D. J. *Gaussian 16*, rev. C.01; Gaussian, Inc.: 2016.
(65) Bochevarov, A. D.; Harder, E.; Hughes, T. F.; Greenwood, J. R.; Braden, D. A.; Philipp, D. M.; Rinaldo, D.; Halls, M. D.; Zhang, J.; Friesner, R. A. Jaguar: A High-performance Quantum Chemistry Software Program with Strengths in Life and Materials Sciences. *Int. J. Quantum Chem.* **2013**, *113*, 2110−2142.
(66) Adamo, C.; Barone, V. Toward Reliable Density Functional Methods without Adjustable Parameters: The PBE0Model. *J. Chem. Phys.* **1999**, *110*, 6158−6170.
(67) Krishnan, R.; Binkley, J. S.; Seeger, R.; Pople, J. A. Self-Consistent Molecular Orbital Methods. XX. A Basis Set for Correlated Wave Functions. *J. Chem. Phys.* **1980**, *72*, 650−654.
(68) McLean, A. D.; Chandler, G. S. Contracted Gaussian Basis Sets for Molecular Calculations. I. Second Row Atoms, Z = 11−18. *J. Chem. Phys.* **1980**, *72*, 5639−5648.
(69) Tomasi, J.; Mennucci, B.; Cammi, R. Quantum Mechanical Continuum Solvation Models. *Chem. Rev.* **2005**, *105*, 2999−3094.
(70) Pelmenschikov, V.; Guo, Y.; Wang, H.; Cramer, S. P.; Case, D. A. Fe-H/D Stretching and Bending Modes in Nuclear Resonant Vibrational, Raman and Infrared Spectroscopies: Comparisons of Density Functional Theory and Experiment. *Faraday Discuss.* **2011**, *148*, 409−420.